

# Fermilab

Oxide-nitride heteroepitaxy for low-loss dielectrics in superconducting quantum circuits

FERMILAB-PUB-26-0206-SQMS

arXiv:2603.29065

This manuscript has been authored by Fermi Forward Discovery Group, LLC under Contract No. 89243024CSC000002 with the U.S. Department of Energy, Office of Science, Office of High Energy Physics.

## **Oxide-nitride heteroepitaxy for low-loss dielectrics in superconducting quantum circuits**

David A. Garcia-Wetten<sup>1,\*</sup>, Mitchell J. Walker<sup>1,\*</sup>, Peter G. Lim<sup>2,\*</sup>, André Vallières<sup>2,3</sup>, Maria G. Jimenez-Guillermo<sup>1,4</sup>, Miguel A. Alvarado<sup>5</sup>, Dominic P. Goronzy<sup>1</sup>, Anna Grassellino<sup>3</sup>, Jens Koch<sup>6,7</sup>, Vinayak P. Dravid<sup>1,8,9,†</sup>, Mark C. Hersam<sup>1,10,11,†</sup>, Michael J. Bedzyk<sup>1,6,†</sup>

<sup>1</sup>Department of Materials Science and Engineering, Northwestern University, Evanston, IL 60208, USA

<sup>2</sup>Graduate Program in Applied Physics, Northwestern University, Evanston, IL 60208, USA

<sup>3</sup>Superconducting Quantum Materials and Systems (SQMS) Division, Fermi National Accelerator Laboratory (FNAL), Batavia, IL 60510, USA

<sup>4</sup>Department of Physics, Elmhurst University, Elmhurst, IL 60126, USA

<sup>5</sup>Department of Chemistry, Northeastern Illinois University, Chicago, IL 60625, USA

<sup>6</sup>Department of Physics and Astronomy, Northwestern University, Evanston, IL 60208, USA

<sup>7</sup>Center for Applied Physics and Superconducting Technologies (CAPST), Northwestern University, Evanston, IL 60208, USA

<sup>8</sup>Northwestern University Atomic and Nanoscale Characterization Experimental (NUANCE) Center, Northwestern University, Evanston, IL 60208, USA

<sup>9</sup>International Institute of Nanotechnology (IIN), Northwestern University, Evanston, IL 60208, USA

<sup>10</sup>Department of Chemistry, Northwestern University, Evanston, IL 60208, USA

<sup>11</sup>Department of Electrical and Computer Engineering, Northwestern University, Evanston, IL 60208, USA

\*These authors contributed equally to this work.

†Corresponding authors: v-dravid@northwestern.edu, m-hersam@northwestern.edu, bedzyk@northwestern.edu

## **Abstract**

Superconducting qubits show great promise for the realization of fault-tolerant quantum computing, but lossy, amorphous dielectrics limit current technology. Identifying highly crystalline and stoichiometric dielectrics with intrinsically low microwave loss is therefore a central materials challenge, yet experimentally validated platforms remain scarce. In this work, we integrate a crystalline dielectric into a heteroepitaxial TiN/ $\gamma$ -Al<sub>2</sub>O<sub>3</sub>/TiN trilayer grown via pulsed laser deposition. Correlative high-resolution imaging, diffraction, and spectroscopy measurements confirm the single-crystal quality and chemical integrity of all layers, with minimal defects and limited anion interdiffusion across the oxide-nitride interfaces. Using microwave lumped-element resonators with parallel-plate capacitors, we report the first direct measurement of the dielectric loss of epitaxial  $\gamma$ -Al<sub>2</sub>O<sub>3</sub>, for which we find a low intrinsic two-level system loss,  $\delta_{\text{TLS}}^0 = (2.8 \pm 0.1) \times 10^{-5}$ . These results establish heteroepitaxial oxides on transition metal nitrides as an attractive materials platform for superconducting quantum circuits, particularly for integration into compact device architectures such as merged-element transmons and microwave kinetic inductance detectors.

## **Main**

Since the proposition<sup>1</sup> and subsequent demonstration<sup>2, 3</sup> of Cooper-pair box qubits, superconducting (SC) qubit technology has accelerated with broad potential for quantum information science (QIS) applications<sup>4</sup>. The incumbent materials choice for the Josephson junctions (JJs) in these devices is amorphous  $\text{AlO}_x$  for the dielectric and Al for the SC electrodes. However, amorphous  $\text{AlO}_x$  as the tunnel barrier is problematic since it hosts parasitic two-level systems (TLSs)<sup>5, 6</sup>, which are a major source of decoherence in SC qubits<sup>7-9</sup>. The lack of long-range order and sub-stoichiometry of amorphous oxides give rise to a wide distribution of atomic coordination geometries<sup>10</sup>, which implies that these defective materials host TLSs with energetically similar configurations to the SC qubits themselves, ultimately compromising coherence<sup>11</sup>. Because single-crystal dielectrics lack the disorder of amorphous materials and thus have a lower density of TLSs, layer-by-layer growth of atomically pristine dielectrics via thin-film epitaxy is an attractive alternative to incumbent amorphous  $\text{AlO}_x$ .

Several material systems have been studied for this purpose. For example, epitaxial semiconductors, such as GaAs<sup>12, 13</sup>, have been used with some success to reduce TLS losses. Another strategy is to fabricate an all-nitride trilayer stack using AlN and transition-metal nitride superconductors<sup>14, 15</sup>. However, both AlN and GaAs are susceptible to higher power-independent losses due to their piezoelectricity<sup>16, 17</sup>. An alternative approach is to form a crystalline  $\text{Al}_2\text{O}_3$  dielectric by depositing at high temperatures. In this strategy, the choice of the SC base layer is key to limiting metal oxidation via interdiffusion with  $\text{Al}_2\text{O}_3$  at elevated growth temperatures<sup>18</sup>. For instance, oxygen interdiffusion at the Nb/ $\text{Al}_2\text{O}_3$  interface precludes the use of Nb for this purpose<sup>19</sup>. Therefore, prior attempts at epitaxial growth of crystalline  $\text{Al}_2\text{O}_3$  have incorporated Re<sup>20</sup> or Re/Ti multilayers<sup>21, 22</sup>, but Re is a suboptimal superconductor for qubit devices due to its poor coherence, low SC energy gap, and high kinetic inductance<sup>23</sup>. Instead, transition metal nitrides stand out as promising superconductors for QIS applications in light of these criteria<sup>24-26</sup>. Towards this end, the growth of  $\text{Al}_2\text{O}_3/\text{NbN}$  trilayers has been investigated, but this approach is limited by oxygen and nitrogen interdiffusion<sup>27</sup>. TiN is particularly attractive in this context because it is a low-loss superconductor that is already widely integrated into QIS technologies<sup>28-34</sup> and related applications, owing to its resistance to oxidation and effectiveness as a diffusion barrier<sup>35, 36</sup>.

SC qubit technology additionally faces a scale-up problem. Conventional transmon qubits coupled via coplanar waveguide (CPW) resonators occupy areas on the order of 2 – 3  $\text{mm}^2$  per device, which limits integration density for many-qubit quantum processing units<sup>37</sup>. Consequently, SC qubits with smaller

footprints are of high interest, but existing designs (e.g., merged-element transmons<sup>38, 39</sup>) have low coherence times that are limited by constituent dielectrics. Prior attempts to address this problem, such as using van der Waals material<sup>40, 41</sup> as the dielectric, while dramatically reducing the device footprint, still rely on techniques incompatible with industrial-scale device fabrication. Consequently, low-loss epitaxial dielectrics grown with wafer-scale compatible thin-film epitaxy are essential not only for improving SC qubit coherence time but also for the development of many-qubit quantum processing units.

Here, we demonstrate the growth of high-quality epitaxial TiN (111)/ $\gamma$ -Al<sub>2</sub>O<sub>3</sub> (111)/TiN (111) trilayers on  $\alpha$ -Al<sub>2</sub>O<sub>3</sub> (001) substrates via pulsed laser deposition (PLD). PLD is chosen because it is a deposition method that has previously yielded high-quality crystalline films of both TiN<sup>42</sup> and Al<sub>2</sub>O<sub>3</sub><sup>43</sup>. In this manner, all three films of the trilayer can be grown in the same deposition system without breaking vacuum or requiring a multi-use system. X-ray reflectivity (XRR), X-ray diffraction (XRD), time-of-flight secondary ion mass spectrometry (ToF-SIMS), and scanning transmission electron microscopy (STEM) are used to characterize layer thicknesses, interfaces, and crystallinities. X-ray photoelectron spectroscopy (XPS) and electron energy-loss spectroscopy (EELS) are further employed to characterize the chemical state of the constituent films. Through these robust structural and spectroscopic measurements, we find that each layer of the stack is highly stoichiometric and crystalline, while collectively maintaining heteroepitaxy, with sharp interfaces and minimal oxygen-nitrogen interdiffusion. To accurately measure the TLS contribution to the intrinsic material loss of epitaxial  $\gamma$ -Al<sub>2</sub>O<sub>3</sub>, we employ a lumped-element resonator<sup>44</sup>, which minimizes the capacitance of the inductor element to ground. By integrating this with a parallel-plate capacitor (PPC) with a filling factor close to unity, TLSs are strongly capacitively coupled in this design, allowing us to attribute the measured TLS losses predominantly to the capacitor dielectric. We test devices with varying dielectric thicknesses to test whether the measurements reflect the bulk  $\gamma$ -Al<sub>2</sub>O<sub>3</sub>'s loss properties or those of the TiN/ $\gamma$ -Al<sub>2</sub>O<sub>3</sub> interfaces. In this manner, we find that the TLS losses of crystalline  $\gamma$ -Al<sub>2</sub>O<sub>3</sub> in the epitaxial trilayer is as low as  $\delta_{\text{TLS}}^0 = (2.8 \pm 0.1) \times 10^{-5}$ , which is two orders of magnitude lower than conventional amorphous AlO<sub>x</sub>. Our lumped-element resonators with an area of  $2.4 \times 10^{-2} \text{ mm}^2$  — a reduction by two orders of magnitude compared to CPW geometries — exhibit exceptionally high quality factors that hold significant promise for emerging QIS applications.

## **Results**

### **Growth and characterization of TiN/ $\gamma$ -Al<sub>2</sub>O<sub>3</sub>/TiN heteroepitaxial trilayers**

Two trilayers of TiN/Al<sub>2</sub>O<sub>3</sub>/TiN are deposited onto c-plane sapphire substrates by PLD. From top to bottom, the first sample (Fig. 1a) is 62.2 nm TiN - 13.5 nm Al<sub>2</sub>O<sub>3</sub> - 53.8 nm TiN, and the second sample (Fig. 1c) is 63.0 nm TiN - 58.3 nm Al<sub>2</sub>O<sub>3</sub> - 68.1 nm TiN, as measured by STEM with  $\pm 0.5$  nm uncertainty. Energy dispersive X-ray spectroscopy (EDS) mapping (Fig. 1b,d) confirms that for both the thin and the thick Al<sub>2</sub>O<sub>3</sub> samples, the elemental distribution is qualitatively as expected, with no significant signs of oxygen in the TiN layers, and that the interfaces are sharp and well-defined.

Epitaxy during PLD growth is verified with reflectance high-energy electron diffraction (RHEED). The RHEED pattern (Fig. 1e) shows vertical streaks with faint spots, indicating some island formation, but predominantly sharp interfaces<sup>45</sup>, consistent with the STEM findings. Layer thicknesses extracted from XRR measurements (Fig. 1f) over a larger area of the two trilayer films is also consistent with STEM measurements: the measured Al<sub>2</sub>O<sub>3</sub> layer thicknesses are 13.5 nm for the first sample (green curve in Fig. 1f) and 58.3 nm for the second sample (blue curve in Fig. 1f). Additionally, the scattering length densities of the TiN and Al<sub>2</sub>O<sub>3</sub> (inset of Fig. 1f) are consistent with their respective theoretical values. Depth-profiling ToF-SIMS of the thick Al<sub>2</sub>O<sub>3</sub> sample (Fig. 1g) also reveals sharp interfaces at both TiN/Al<sub>2</sub>O<sub>3</sub> interfaces and minimal interdiffusion between the layers. The peak in the TiNO<sup>+</sup> signal at 0 s of etch time is consistent with a thin layer of oxidized TiN at the top of the trilayer stack, which is exposed to air.

To investigate the crystal structures and epitaxial relationships of all layers, we perform high-resolution STEM and high-resolution XRD. Annular bright-field (ABF-)STEM images (Figs. 2a-c) of the trilayers additionally demonstrate that both TiN layers have the expected rock salt structure in the (111) specular orientation (insets in Figs. 2a,c), and in particular, that the bottom TiN layer grows epitaxially to the c-plane sapphire substrate. Both TiN/Al<sub>2</sub>O<sub>3</sub> interfaces are also flat and epitaxial, albeit with some roughness attributed to anion interdiffusion, as discussed later. Of note, the alumina (Fig. 2b) is a single-crystal with the cubic  $\gamma$ -Al<sub>2</sub>O<sub>3</sub> phase, in contrast to the hexagonal-R  $\alpha$ -Al<sub>2</sub>O<sub>3</sub> sapphire substrate, as evidenced by the appearance of superlattice peaks in the fast Fourier transform (FFT) patterns (inset in Fig. 2b) and four-dimensional (4D-)STEM diffraction patterns (Fig. S1e). The  $\gamma$ -Al<sub>2</sub>O<sub>3</sub> phase is a defective spinel-like cubic  $Fd\bar{3}m$  crystal with both tetrahedral and octahedral coordination of the Al sites, enabled by ordered oxygen vacancies<sup>46</sup>, which grows epitaxially on cubic  $Fm\bar{3}m$  TiN crystals at elevated temperatures (Fig. 2d).

XRD provides further information on the heteroepitaxial relationship of the TiN and  $\gamma$ -Al<sub>2</sub>O<sub>3</sub> layers. First, referring to the specular scattering pattern (purple curve in Fig. 2e), the TiN (111) and (222) appear at  $Q = 2.56 \text{ \AA}^{-1}$  and  $5.10 \text{ \AA}^{-1}$ , respectively. The  $\gamma$ -Al<sub>2</sub>O<sub>3</sub> (222) and (444) are present at  $Q = 2.75 \text{ \AA}^{-1}$  and  $5.48 \text{ \AA}^{-1}$ , but the (333) is missing. This omission is not unprecedented in epitaxial  $\gamma$ -Al<sub>2</sub>O<sub>3</sub> thin films and may arise from stabilized cation ordering not present in the bulk crystal structure<sup>47</sup>. The peak at  $Q = 3.08 \text{ \AA}^{-1}$  is TiN (002). This “impurity” orientation is present only in the top TiN layer, as shown by virtual dark-field images in the 4D-STEM measurements (Fig. S1f,g).

Off-specular, radial  $Q$  scans (green curves in Fig. 2e) confirm the cubic structure of  $\gamma$ -Al<sub>2</sub>O<sub>3</sub>. At an elevation of  $54.7^\circ$  in the cubic [110] direction, the TiN (220) appears at  $Q = 2.41 \text{ \AA}^{-1}$ , as well as  $\gamma$ -Al<sub>2</sub>O<sub>3</sub> (220) and (440) at  $Q = 2.25 \text{ \AA}^{-1}$  and  $4.50 \text{ \AA}^{-1}$ , respectively. At an elevation of  $35.3^\circ$  in the cubic [001] direction, the TiN (002) is visible at  $Q = 2.96 \text{ \AA}^{-1}$ , and the  $\gamma$ -Al<sub>2</sub>O<sub>3</sub> (004) is visible at  $3.18 \text{ \AA}^{-1}$ . Additionally, the  $\gamma$ -Al<sub>2</sub>O<sub>3</sub> (113) is observable at an elevation of  $60.5^\circ$  and  $Q = 2.62 \text{ \AA}^{-1}$ . This peak is a superlattice reflection from the superstructure of ordered Al tetrahedral and octahedral sites in the  $\gamma$ -Al<sub>2</sub>O<sub>3</sub> structure. All of these peaks are observed to have 6-fold symmetry about the specular direction, indicating a  $180^\circ$ -twin (Fig. 2f). This twinning is expected for cubic (111)/sapphire (001) epitaxy, which may arise because of alternating A-B stacking from step-to-step on the sapphire surface.

Chemical-state characterization of the trilayer stacks is performed using XPS and EELS. The surface XPS scans (dark blue curves in Fig. 3a) show that the top surface is composed of TiN, reflected by the strong first doublet in the Ti 2p spectrum (the “TiN doublet”) and the tallest peak at 395 eV in the N 1s spectrum<sup>48</sup>. The TiN doublet is separated from the N 1s signal by 57.7 eV, indicative of TiN with some N deficiency<sup>49</sup>. This observation is consistent with the prominent TiO<sub>x</sub> peak shifted by 3.1 eV from the TiN doublet and the strong O 1s signal<sup>50</sup>; these features are attributable to oxidation of the TiN surface from ambient exposure, in agreement with the ToF-SIMS data (Fig. 1g). The remaining peaks involved in the Ti 2p fitting can be interpreted as two Ti<sub>x</sub>O<sub>y</sub>N<sub>z</sub> doublets (based on their separations of 1.1 eV and 2.3 eV from the TiN doublet)<sup>50</sup>, shake-up satellite features, surface plasmon loss features, and bulk plasmon loss features. The shake-up peaks are fixed at 1.9x the area of the TiN peaks, with splitting according to Jaeger *et al.*<sup>48</sup>. Two additional peaks are added to fit the shoulders in the N 1s spectrum: the 393.7 eV peak is associated with TiON<sup>50</sup>, while the 396.1 eV peak could not be assigned.

XPS can also probe the bulk and buried interfaces by sputtering the surface with Ar<sup>+</sup> ions between successive scans. The magenta curves in Fig. 3a show XPS results taken at a depth midway through the top TiN layer. Referring to the Ti 2p and N 1s spectra, the ratio of Ti<sub>x</sub>O<sub>y</sub>N<sub>z</sub> and TiO<sub>x</sub> signal intensities to

those of TiN is much weaker compared to the same ratios in the dark blue, surface-level XPS curves. Likewise, the O 1s signal coming from the bulk TiN is much weaker than the dark blue, surface-level O 1s signal. These findings are corroborated with elemental quantification, which indicates that the TiN bulk is close to stoichiometric with just 8 at.% O. This oxygen concentration is slightly higher than we would expect based on our SC transition temperature ( $T_c$ ) measurement of 4.8 K (Fig. S2), so we hypothesize that this percentage is an over-estimate due to Ar<sup>+</sup> ion milling damage and oxygen gettering in the high (but not ultrahigh) vacuum XPS chamber<sup>51</sup>.

The cyan curves in Fig. 3a show XPS from a depth in the center of the  $\gamma$ -Al<sub>2</sub>O<sub>3</sub> layer. Here, the Al 2p and O 1s signals dominate, as expected, with the Ti 2p and N 1s signals having disappeared almost entirely. No shoulders from metal oxides are present in the O 1s spectrum. Elemental quantification confirms that the  $\gamma$ -Al<sub>2</sub>O<sub>3</sub> is highly stoichiometric.

Further interrogation of the chemical state of the  $\gamma$ -Al<sub>2</sub>O<sub>3</sub> and its interfaces with the TiN is performed using EELS. The EELS data (Fig. 3b) correspond to the N-K edge, Ti-L<sub>2,3</sub> edge, and O-K edge measured along the vertical direction of the dielectric and are color-matched with the ABF-STEM image (Fig. 3c). The Ti-L<sub>2,3</sub> edge shape throughout the TiN in proximity to the  $\gamma$ -Al<sub>2</sub>O<sub>3</sub> is predominantly of Ti<sup>3+</sup>, corresponding to highly stoichiometric TiN. There are no signs of a significant Ti-L<sub>2,3</sub> edge shift or splitting indicative of Ti<sup>4+</sup> nor an O-K edge field splitting into the  $t_{2g}$  and  $e_g$  levels, which would indicate formation of TiO<sub>2</sub><sup>52</sup>. These findings confirm that the TiN layer is chemically resistant to oxidation, unlike many other standard SC electrodes used in qubits. Furthermore, the O-K edge spectrum throughout the bulk of the dielectric layer is in good agreement with the known spectrum of  $\gamma$ -Al<sub>2</sub>O<sub>3</sub>, with an edge shape clearly distinct from the O-K spectrum of  $\alpha$ -Al<sub>2</sub>O<sub>3</sub><sup>53, 54</sup>, providing further corroboration of the identification of the Al<sub>2</sub>O<sub>3</sub> as gamma phase.

Despite largely clean and flat interfaces, the splitting of the O-K edge into two peaks at ~541 eV and ~539 eV at both interfaces with the TiN resembles electronic transitions into mixed states of the O 2p and Al  $t_{2g}$  and  $e_g$  states, corresponding to both tetrahedral and octahedral coordination of the Al sites, suggesting increasingly disordered oxygen vacancy sites near the interfaces. An additional extended energy-loss fine structure at ~549 eV arises from transitions into mixed states of the O 2p and the Al 3s and 3p state<sup>50, 53, 55</sup>. These measurements additionally reveal the formation of ~1.5 nm thin Ti<sub>x</sub>O<sub>y</sub>N<sub>z</sub> interlayers at both TiN/ $\gamma$ -Al<sub>2</sub>O<sub>3</sub> interfaces, as observed by the coexistence of N-K, Ti-L<sub>2,3</sub>, and O-K edges over a non-negligible region along the interfaces. These Ti<sub>x</sub>O<sub>y</sub>N<sub>z</sub> interlayers can be attributed to oxygen migration from  $\gamma$ -Al<sub>2</sub>O<sub>3</sub>, evident from the appearance of an O-K pre-edge at ~532 eV indicating oxygen

deficiency in  $\gamma\text{-Al}_2\text{O}_3$ , and the appearance of a secondary N-K edge at  $\sim 400$  eV representing displaced nitrogen atoms dissolved as unbonded nitrogen in the matrix<sup>56</sup>. It is possible that some diffusion occurred at elevated temperatures during PLD deposition, which may explain the faint diffuseness visible at both interfaces in ABF-STEM images (Figs. 2a-b).

### Dielectric loss extraction of epitaxial $\gamma\text{-Al}_2\text{O}_3$

To obtain an accurate measurement of the dielectric loss of epitaxial  $\gamma\text{-Al}_2\text{O}_3$ , lumped-element resonators with parallel-plate capacitors (LEPPCs) are designed, simulated, and fabricated. This device design concentrates the electric field in the PPCs, such that the majority of losses observed are dominated by either the bulk of the dielectric or its interfaces with the TiN layers. As depicted in Fig. 4a, starting from a trilayer blanket film, the top TiN and the  $\gamma\text{-Al}_2\text{O}_3$  are first patterned and etched into a circular-shaped capacitor. A second patterning and etching step defines the inductor, ground plane, and the feedline in the bottom TiN layer. An Al air bridge is used to connect the top electrode of the capacitor to the inductor, rather than an insulating spacer, to limit dielectric losses outside the capacitor dielectric<sup>13, 57</sup>. Details of the fabrication are provided in the Methods and Supplementary Information. The resulting devices, as shown in scanning electron microscopy (SEM) images (Figs. 4b-c), exhibit high fidelity to the desired device geometry, with no observable photoresist or other residue. The slight waviness on either side of the air bridge pictured in Fig. 4b is likely due to the laser of the direct optical writer having imperfect focus over variations in sample height during photolithography. The interface between the trilayer and the Al air bridge is also sharp and free of oxygen and carbon residues (Fig. S4). Fig. 4d shows a simulation of the electric field distribution in the LEPPC device, derived from finite element modeling (FEM). The FEM model shows that the field is strongly concentrated in the PPC, with a filling factor near unity. Therefore, the measured TLS loss of the entire device can be attributed to the intrinsic material TLS loss of the capacitor dielectric, assuming TLSs are only capacitively coupled<sup>44</sup>.

After fabrication, the LEPPC devices are loaded into a dilution refrigerator at 10 mK for microwave testing, with the results shown in Fig. S5. At low power, devices fabricated with the thin (13.5 nm) and the thick (58.3 nm)  $\gamma\text{-Al}_2\text{O}_3$  perform similarly: the thick  $\gamma\text{-Al}_2\text{O}_3$  device has a low-power total loss  $\delta_{LP}$  of  $(3.6 \pm 0.3) \times 10^{-5}$ , while the thin  $\gamma\text{-Al}_2\text{O}_3$  device has a  $\delta_{LP}$  of  $(3.2 \pm 0.2) \times 10^{-5}$ . The fact that the  $\delta_{LP}$  values measured for each condition are similar suggests that the low-power loss properties of these devices are significantly influenced by the bulk of the  $\gamma\text{-Al}_2\text{O}_3$ , with marginal contributions from interfacial loss mechanisms at the TiN/ $\gamma\text{-Al}_2\text{O}_3$  interfaces, such as the thin  $\text{Ti}_x\text{O}_y\text{N}_z$  interlayers.

Furthermore, the volume of the dielectric material being tested in each device is sufficiently large, such that the number of TLSs actually present is expected to match the theoretical TLS density for this material in the bulk limit. Therefore, these  $\delta_{LP}$  values represent an upper bound of the low-power material loss of the  $\gamma$ -Al<sub>2</sub>O<sub>3</sub> itself. We can also extract the intrinsic TLS loss,  $\delta_{TLS}^0$ , for  $\gamma$ -Al<sub>2</sub>O<sub>3</sub> of both thicknesses, which we find to be  $(3.5 \pm 0.2) \times 10^{-5}$  and  $(2.8 \pm 0.1) \times 10^{-5}$  for the thick and thin  $\gamma$ -Al<sub>2</sub>O<sub>3</sub> layers, respectively. Based on our device design, these measured TLS loss values reflect the intrinsic dielectric loss of the  $\gamma$ -Al<sub>2</sub>O<sub>3</sub> dielectric material.

At high powers, we observe exceptionally large high-power quality factors, with  $Q_{max} = (6.4 \pm 0.5) \times 10^5$  for the thick  $\gamma$ -Al<sub>2</sub>O<sub>3</sub> device and  $Q_{max} = (2.7 \pm 0.1) \times 10^5$  for the thin  $\gamma$ -Al<sub>2</sub>O<sub>3</sub> device, before the resonator response becomes non-linear. The significant difference in performance at high power suggests a power-independent loss mechanism dominated by the interfaces. This loss could be associated with the thin nonstoichiometric Ti<sub>x</sub>O<sub>y</sub>N<sub>z</sub> layer at the TiN/ $\gamma$ -Al<sub>2</sub>O<sub>3</sub> interfaces observable by EELS and XPS (Fig. 3). Another possibility is that the loss could be associated with the twinned TiN domains revealed by 4D-STEM measurements (Fig. S1f,g).

Table I compares these performance metrics with those of other dielectrics reported in the literature. Inclusion in this table is limited to measurements using integrated PPC-type geometries to keep comparisons meaningful; otherwise, filling factors and extraction protocols may differ widely. In general, AlO<sub>x</sub> can exhibit a wide range of loss values, depending on deposition technique, crystallinity, stoichiometry, and potentially other factors. Since most state-of-the-art JJs consist of amorphous AlO<sub>x</sub> formed by oxidizing electron-beam-deposited Al, among the reports listed in Table I, Zotova *et al.*<sup>58</sup> is arguably the most relevant for understanding the loss properties of the amorphous AlO<sub>x</sub> most often employed in contemporary JJs. Of the ten loss measurements collected by Zotova *et al.* from LEPPCs with Al-AlO<sub>x</sub>-Al capacitors, the average  $\delta_{LP}$  is  $1.44 \times 10^{-3}$ , or an approximate  $F\delta_{TLS}^0$  of  $1.42 \times 10^{-3}$ . The epitaxial PLD  $\gamma$ -Al<sub>2</sub>O<sub>3</sub> presented here, therefore, represents an improvement of nearly two orders of magnitude over the incumbent JJ material in terms of low-power intrinsic material loss, consistent with other reports of epitaxial Al<sub>2</sub>O<sub>3</sub> listed in Table I.

## **Discussion**

In this work, we have presented an epitaxial TiN/ $\gamma$ -Al<sub>2</sub>O<sub>3</sub>/TiN trilayer materials stack. The materials and device preparation process starts with the PLD heteroepitaxy of TiN on sapphire. By baking and titanium-gettering the PLD chamber to reduce the water and oxygen content prior to deposition, as detailed in the Methods, we deposit near-stoichiometric TiN. XPS depth profiling, EDS mapping, and ToF-SIMS depth profiling reveal a low concentration of oxygen and Ti<sub>x</sub>O<sub>y</sub>N<sub>z</sub> species in the bulk of the TiN. Electron and X-ray diffraction of the TiN confirm excellent crystallinity and epitaxy with the sapphire substrate. Furthermore, the measured  $T_c$  of TiN at 4.8 K (Fig. S2) is consistent with the highest reported  $T_c$  of PLD-grown TiN on sapphire<sup>42</sup>. These materials properties make the initial TiN film an ideal platform for the further deposition of the trilayer by PLD.

Multimodal materials characterization confirms the growth of a cubic  $Fd\bar{3}m$   $\gamma$ -phase of Al<sub>2</sub>O<sub>3</sub> and heteroepitaxy throughout the stack. Each layer in the trilayer exhibits high crystallinity, with a consistent epitaxial relationship throughout the stack and sharp interfaces. In particular, minimal structural and chemical disorder is observed in the crystalline, stoichiometric dielectric. While some oxidation of the TiN is present at the superconductor-dielectric interface, the Ti<sub>x</sub>O<sub>y</sub>N<sub>z</sub> interlayer thicknesses are limited to 1 – 2 nm, and there is negligible diffusion of oxygen from the  $\gamma$ -Al<sub>2</sub>O<sub>3</sub> layer into the TiN bulk, demonstrating the diffusion-barrier properties of TiN.

By integrating this trilayer into LEPPC devices with air bridges, we enable measurements of the microwave loss properties of  $\gamma$ -Al<sub>2</sub>O<sub>3</sub>. The intrinsic material TLS loss of  $\gamma$ -Al<sub>2</sub>O<sub>3</sub> is found to be  $\delta_{\text{TLS}}^0 = (2.8 \pm 0.1) - (3.5 \pm 0.2) \times 10^{-5}$ , representing an improvement by two orders of magnitude compared to the amorphous AlO<sub>x</sub> used in conventional JJs. With this exceptionally low TLS loss, this materials system is a strong candidate for merged-element transmon devices<sup>38,39</sup>. In addition, the low loss at high microwave powers further suggests that this materials system can benefit additional superconducting applications such as microwave kinetic inductance (MKID) devices<sup>59,60</sup>.

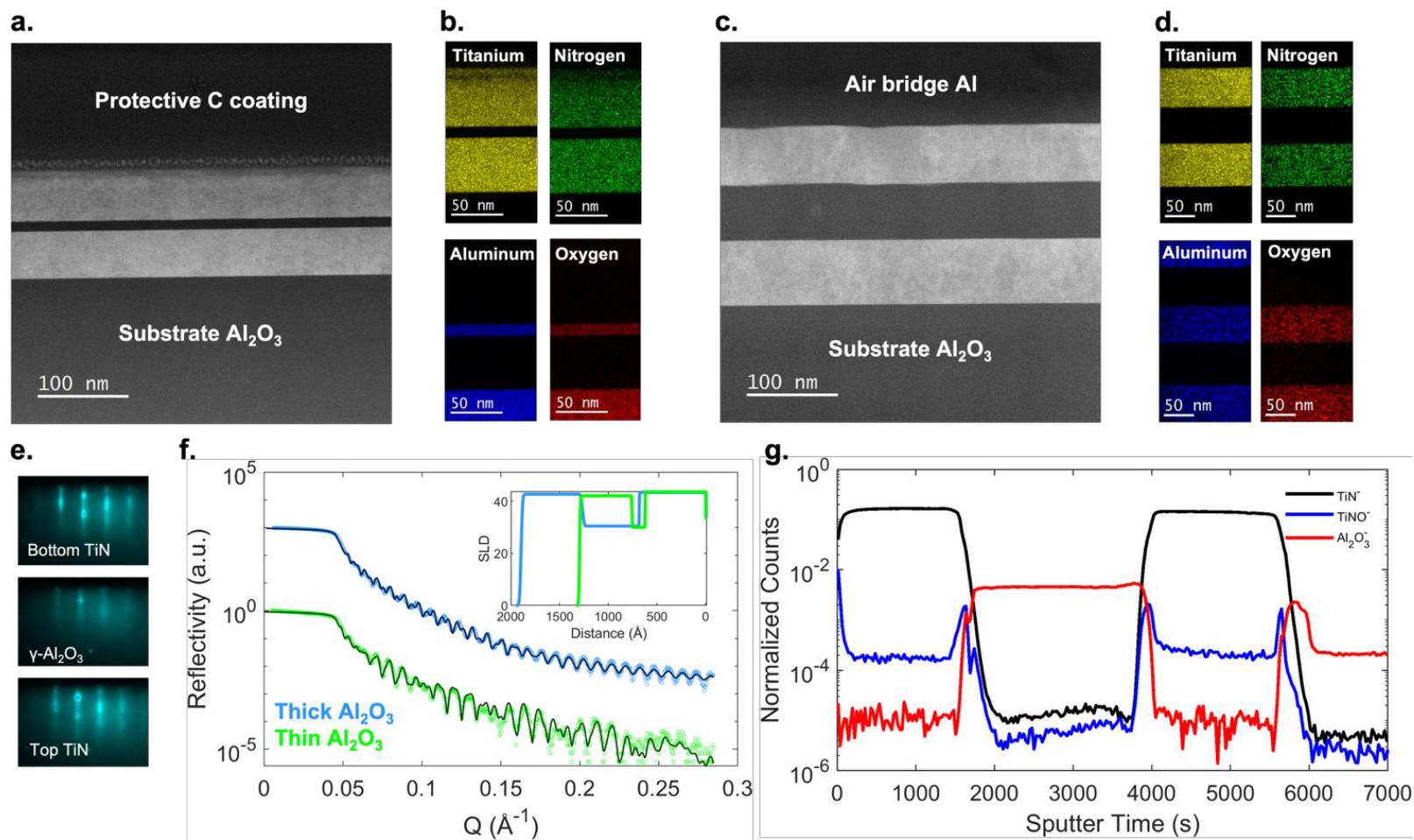


**Fig. 1: Materials characterization of PLD-deposited TiN-Al<sub>2</sub>O<sub>3</sub>-TiN trilayers.**

**a,c**, HAADF-STEM images and **b,d**, EDS maps of the thin and thick trilayer samples, showing well-defined, elementally homogeneous layers with flat interfaces. **e**, *in situ* RHEED of the surface of the bottom TiN, middle Al<sub>2</sub>O<sub>3</sub>, and top TiN layers, showing epitaxial matching with some island growth. **f**, XRR of the thin and thick trilayer samples. The inset shows the scattering-length density profile from the fits. **g**, ToF-SIMS depth profile of the thick trilayer sample, showing the depth-distribution of TiN<sup>-</sup>, TiNO<sup>-</sup>, and Al<sub>2</sub>O<sub>3</sub><sup>-</sup> species.

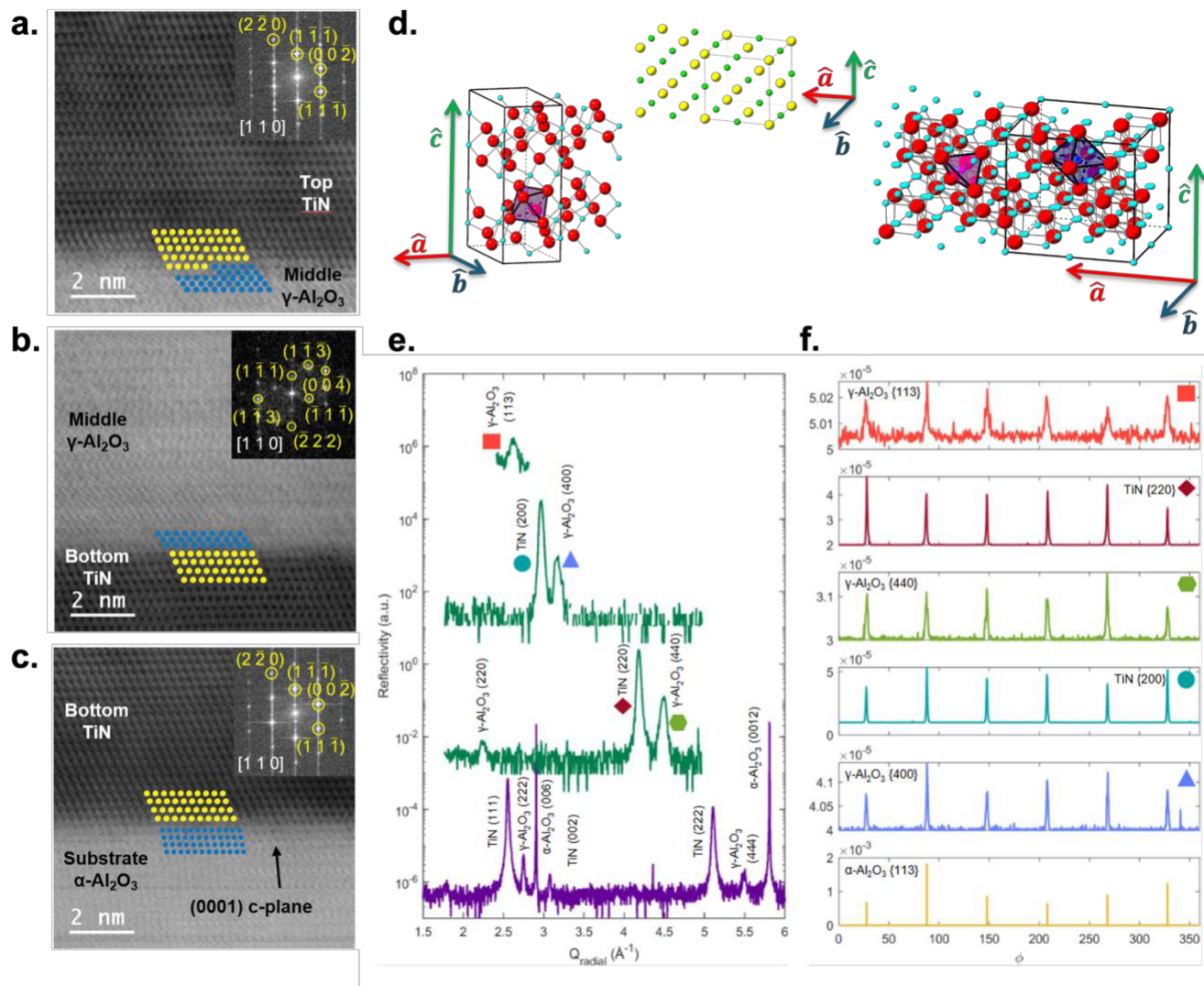


**Fig. 2: Crystal structure and heteroepitaxy of TiN/ $\gamma$ -Al<sub>2</sub>O<sub>3</sub>/TiN.**

**a-c**, Atomic-resolution ABF-STEM images of the interfaces between each film layer and the substrate, demonstrating heteroepitaxy and high-quality interfaces. The insets show FFT patterns of the individual layers, with the zone axes and diffraction peaks identified and labeled. **d**, Simulated crystal structures of the substrate and films. **e**, Specular (purple) and off-specular, radial Q (green) XRD scans of the thick trilayer sample, and **f**,  $\phi$  scans of selected XRD peaks, showing the rotational symmetry and epitaxial matching of the film layers.

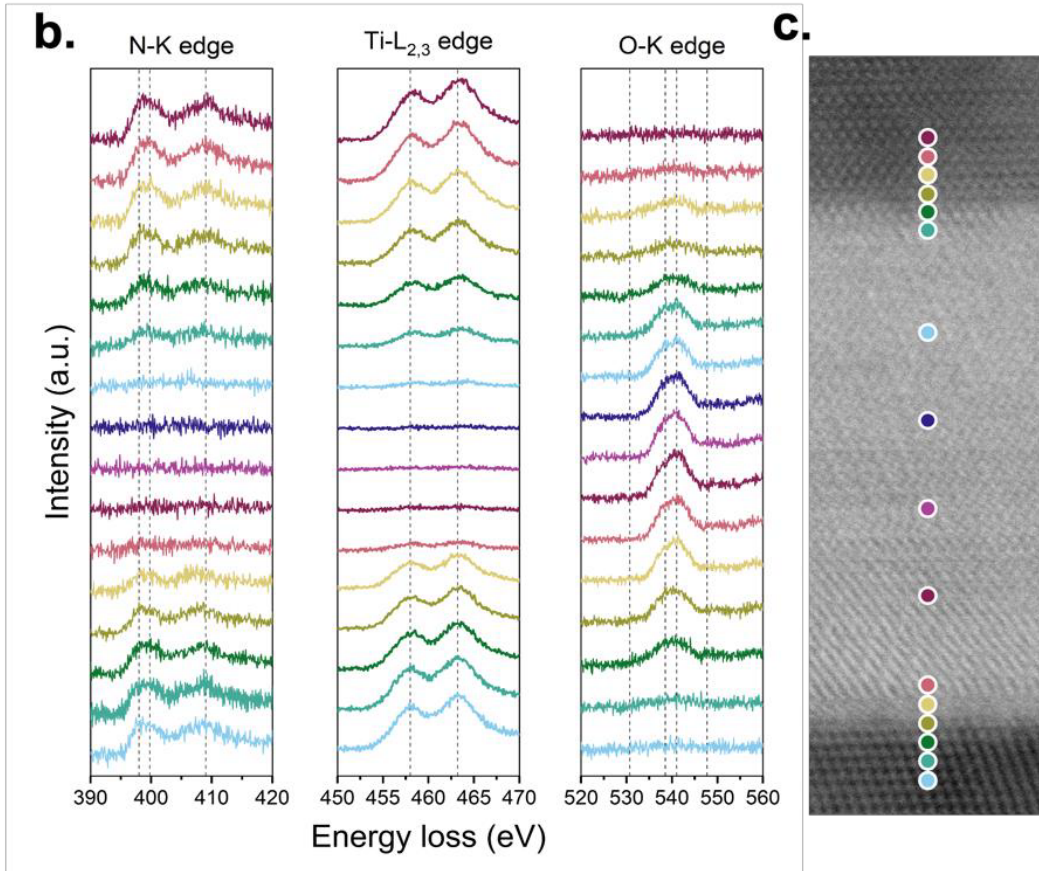
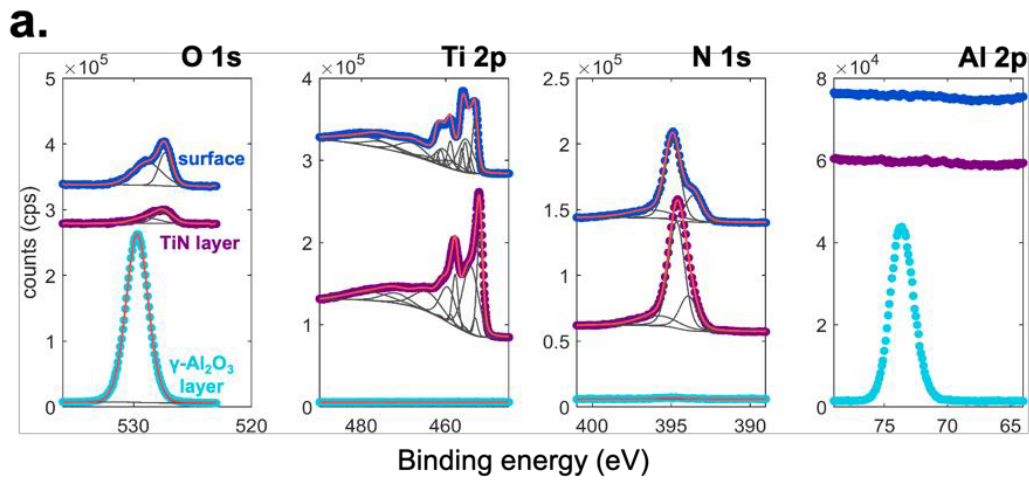


**Fig. 3: Chemical analysis at the TiN/ $\gamma$ -Al<sub>2</sub>O<sub>3</sub> interfaces.**

**a**, XPS of core-level emissions of the thick trilayer sample. Buried layers were probed using an Ar<sup>+</sup> ion beam. **b**, Core-loss EELS along the two interfaces between the TiN layers and  $\gamma$ -Al<sub>2</sub>O<sub>3</sub> film, with **c**, an ABF-STEM image indicating the location of these spectra.

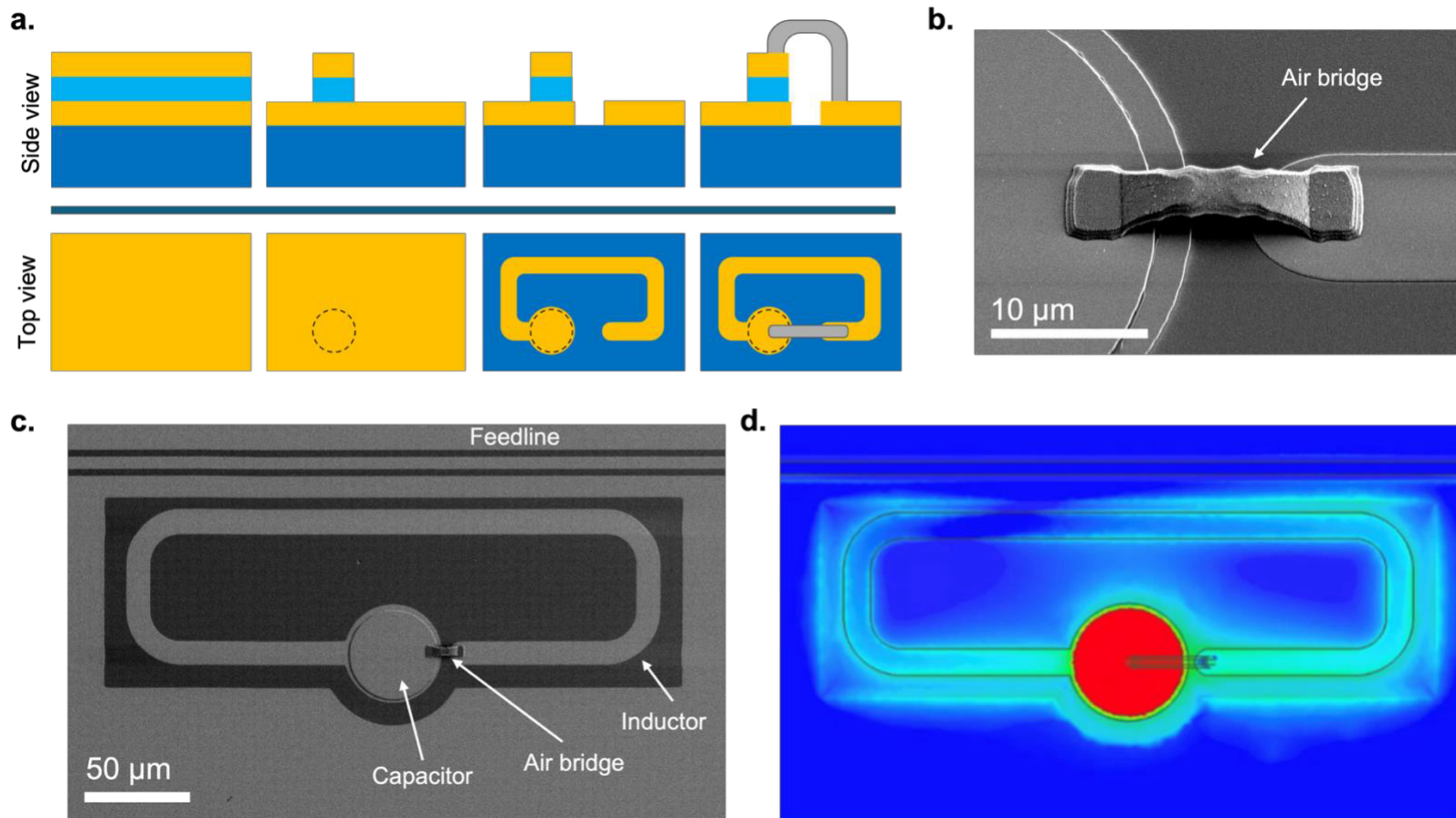


**Fig. 4. LEPPC device overview.**

**a**, Schematic of LEPPC device fabrication procedure, where the top TiN (yellow) and dielectric  $\gamma\text{-Al}_2\text{O}_3$  (light blue) are optically defined to be the PPC, and the bottom TiN (yellow) comprises the LE resonator, along with an aluminum airbridge (grey) completing the LC circuit. **b**, Tilted SEM image of a representative airbridge, and **c**, top-down SEM image of a representative LEPPC device. **d**, FE modeling of the same device, displaying the electric field distribution upon microwave measurements concentrated in the PPC region. The color scale corresponds to the strength of the electric field on a logarithmic scale with arbitrary units (red - high, blue - low).

Material	Ref.	Deposition	Crystallinity	Geometry	$\delta_{LP}$ (x $10^{-5}$ )	$F\delta_{TLS}^0$ (x $10^{-5}$ )	$Q_{max}$ (x $10^5$ )	Area (x $10^5 \mu m^2$ )
thick $\gamma$ - $Al_2O_3$	This work	PLD	epitaxial	LEPPC	$3.6 \pm 0.3$	$3.5 \pm 0.2$	$6.4 \pm 0.5$	0.244
thin $\gamma$ - $Al_2O_3$	This work	PLD	epitaxial	LEPPC	$3.2 \pm 0.2$	$2.8 \pm 0.1$	$2.7 \pm 0.1$	0.244
$Al_2O_3$	21	MBE	epitaxial	LEPPC	6			0.055
$Al_2O_3$	20	PLD	epitaxial	LEPPC	3–5	2.3–4.3*	1.4	
$Al_2O_3$	44	sputter	amorphous	LEPPC	93.7*	92	0.59	1.225
$Al_2O_3$	60	ALD	amorphous	LEKID	†	†	1.5	0.0952
$AlO_x$	61	plasma ox.	amorphous	LE overlap	140–175	139–174*	1	0.075–0.1155
$AlO_x$	62	anodic ox.	amorphous	CPWPPC	4–22*	4–22	8	20
$AlO_x$	39	e-beam evap.	amorphous	Mergemon	$\leq 0.05$	$\leq 0.047$		
$AlO_x$	58	e-beam evap.	amorphous	LEPPC	144	142*	0.45	0.4
GaAs	13	MBE	epitaxial	LEPPC	11.2*	6.4	0.21	1.404
hBN	41	flake transfer	single crystal	LEPPC	0.29–0.53	0.14–0.38*	2.7–6.8	6.25
hBN	40	flake transfer	single crystal	vdW transmon	2.8			45
$Nb_2O_5$	63	anodic ox.	amorphous	LEPPC	†	†	$\leq 0.01$	7
Si	64	sputter	amorphous	LEPPC	150–200	140–190*	0.1	1–3
Si	65	PECVD	amorphous	LEPPC	15–50			1.8
Si	66	ICPCVD	amorphous	LEPPC	5.3–9.3*	4–8	0.8	3.9
Si	67	Si wafer	epitaxial	LEIDC w/ fins	0.56–1.2			1.75
Si	68	SOI wafer	single crystal	LEPPC	0.54	0.43*	9	3
Si:H	69		amorphous	LEPPC		$F \times (2.2–2.5)$	9.1	
SiC:H	70	PECVD	amorphous	LEPPC		$F \times (2–6)$	5	0.3
$Si_3N_4$	66	ICPCVD	amorphous	LEPPC	98–111*	97–110	1.3	3.9
$Si_3N_4$	71	LPCVD	amorphous	MKID w/ $\mu$ -strip		200		62.5
$SiN_x$ :H	72	ICPCVD	amorphous	LEPPC		$F \times (2.5–120)$	2	0.252
$SiN_x$	7	CVD	amorphous	LEPPC	20	19*	1.25	

SiN <sub>x</sub>	69		amorphous	LEPPC / CPW	10–20	10–20*	5.3	
SiN <sub>x</sub>	64	ECR-PECVD	amorphous	LEPPC	40–50	40–50*	5.9	1–3
SiN <sub>x</sub>	63	PECVD	amorphous	LEPPC	†	†	0.033–0.1	7
SiN <sub>x</sub>	73	PECVD	amorphous	LEPPC		F × 78		0.7
SiN <sub>x</sub>	66	ICPCVD	amorphous	LEPPC	4.5–16*	4–15	2.0	3.9
SiN <sub>x</sub>	74	LPCVD	amorphous	MKID w/ $\mu$ -strip	183–218*	180–215	0.3	
SiO	63	thermal evap.	amorphous	LEPPC	†	†	0.02–0.05	7
SiO	75	thermal evap.	amorphous	LEPPC	9.5–37	3.6–31*	0.17	
SiO <sub>2</sub>	7	CVD	amorphous	LEPPC	500	494*	0.17	
SiO <sub>2</sub>	64	ECR-PECVD	amorphous	LEPPC	600	599*	1	1–3

**Table I. Summary of microwave loss measurements of relevant dielectrics from literature, measured in device geometries involving an integrated PPC.**

Columns from left to right: dielectric material under measurement (Material); reference reporting the measurement (Ref.); technique by which the material was obtained (Deposition); crystalline properties of the material under measurement (Crystallinity); device geometry in which the material was measured (Geometry); low-power intrinsic loss ( $\delta_{LP}$ ); resonator-induced intrinsic TLS loss ( $F\delta_{TLS}^0$ ); maximum intrinsic quality factor ( $Q_{max}$ ); *approximate* footprint of a single device in its totality, including both the capacitor and the resonator to which it is coupled (Area). Items were left blank if the reference did not report the information. The crystallinity of the material is assumed to be amorphous unless explicitly stated and shown otherwise. Asterisks (\*) indicate estimates based on the data reported by the reference, such as extracting  $F\delta_{TLS}^0$  from  $\delta_{LP}$  measurements and provided S-curves, or vice versa. Daggers (†) indicate items for which no comparable data were reported (e.g., having large deviations of measured power or temperature from our work). While some reports of amorphous AlO<sub>x</sub> have comparable or even lower  $\delta_{LP}$  values than the epitaxial Al<sub>2</sub>O<sub>3</sub> reported in this work, direct comparison of these results to one another and to the result reported here is confounded by several factors. Readers are directed to the Supplementary Information for discussion of the nuances of these comparisons.

## **Methods**

### **Pulsed laser deposition (PLD), Reflection high-energy electron diffraction (RHEED)**

Pulsed laser deposition of the TiN and Al<sub>2</sub>O<sub>3</sub> films was performed using a 248 nm, 20 Hz pulsed laser with a pulse energy of 340 mJ, and a spot size of 1 × 2 mm<sup>2</sup>. The 2-inch α-Al<sub>2</sub>O<sub>3</sub> (001) substrates were first annealed in air at 1100°C for 2 hours. The deposition of each layer was performed at 750°C, at a background pressure for the TiN of 3 × 10<sup>-4</sup> Torr N<sub>2</sub> and at the chamber base pressure for the Al<sub>2</sub>O<sub>3</sub>. Ablation of a TiN target with an ultraviolet laser can cause incomplete ablation and the ejection of particles onto the wafer. It was found that this process is mitigated in the first 40,000 pulses of a freshly polished target, so multiple freshly polished TiN targets on a carousel were switched to achieve the desired thickness, free of particles. These films were grown in high-vacuum chambers typically used for PLD of oxides, which poses a challenge for oxygen-free TiN growth. The chamber was baked by operating the substrate heater at 900°C for 20 hours while ablating a titanium target at 20 Hz and 200 mJ to getter O<sub>2</sub> and H<sub>2</sub>O. The residual gas during this process was tracked with a residual gas analyzer. After baking, the substrate was introduced into the deposition chamber via the load-lock. This process is based on the work of Torgovkin *et al.*<sup>42</sup>. Without this baking process, the O content of TiN was 25 at%, and we could not measure a SC transition.

### **X-ray reflectivity (XRR), High-resolution X-ray diffraction (HRXRD)**

X-ray reflectivity and high-resolution X-ray diffraction were performed on a Rigaku SmartLab diffractometer using monochromated (double-bounce Ge (220)) Cu Kα<sub>1</sub> radiation. XRR was fit using the Python-based refnx analysis package<sup>76</sup>.

### **Time-of-flight secondary ion mass spectrometry (ToF-SIMS)**

ToF-SIMS data were collected on a blanket trilayer sample with thick γ-Al<sub>2</sub>O<sub>3</sub> using a dual beam IONTOF M6. Negatively charged secondary ions were collected with a Bi<sup>+</sup> ion beam produced by a liquid metal ion gun (LMIG) operated at 30 keV, with an analysis area of 49 × 49 μm<sup>2</sup>. Concurrently with the LMIG, a Cs<sup>+</sup> ion gun was directed at the sample, operated at 0.5 keV, with a sputtering area of 200 × 200 μm<sup>2</sup>, to obtain a depth profile. SurfaceLab7 software was used to plot and analyze the SIMS data.

### **Scanning transmission electron microscopy (STEM), Energy-dispersive X-ray spectroscopy (EDS), Electron energy-loss spectroscopy (EELS), Four-dimensional STEM (4D-STEM)**

Cross-sectional lamella samples were prepared by Xe<sup>+</sup> plasma focused ion beam (FIB) using the Thermo Scientific Helios 5 Hydra CX DualBeam Plasma FIB/SEM. Bulk-out, lift-out, and thinning processes were performed using 30 kV Xe<sup>+</sup> ion beam. Final surface cleaning steps were performed at 8 kV and 5 kV. Samples were then polished using Fischione Model 1040 NanoMill at 1 – 0.5 kV and plasma-cleaned using South Bay Technology PC-2000 Plasma Cleaner with Ar<sup>+</sup> plasma at 20 – 40 W RF power for 15 s at 150 mTorr to remove residual contamination.

STEM data were collected on an aberration-corrected JEOL JEM-ARM200CF S/TEM operating at 200 kV. The STEM convergence angle, high-angle annular dark field (HAADF) collection angle, and ABF collection angle were 27 mrad, 90 – 370 mrad, and 23 mrad, respectively. EDS data were collected in the same microscope at 200 kV with Thermo Fisher dual silicon-drift EDS detectors (1.7 steradians). EELS and 4D-STEM data were collected on a JEOL JEM-ARM300F GrandARM S/TEM operating at 300 kV with the Gatan GIF Continuum filter with K3 IS direct electron detector. The EELS collection camera length was 2 cm, with a high-resolution aperture of 2.5 mm. The energy dispersion was set to 90 meV/Ch to ensure the high energy resolution necessary for probing small peak shifts and splitting. A wide energy slit of 500 eV width was inserted to record the inner-shell edges in the core-loss spectrum while limiting spectrometer aberrations. 4D-STEM convergence angle was set to be 0.5 – 1.5 mrad, with a collection camera length of 4 cm. A narrow energy slit of 20 eV width was inserted to minimize diffuse inelastic scattering to maximize contrast in the collected nanobeam diffraction. A step size of 5 Å was selected to ensure high spatial resolution while avoiding oversampling. Data processing (background subtraction, denoising, signal mapping and analysis, plural scattering removal, virtual imaging, Bragg disk detection, probe calibration, geometric phase analysis for strain mapping) was performed using the Gatan Microscopy Suite software.

### **X-ray photoelectron spectroscopy (XPS)**

XPS data were collected with a Thermo Scientific ESCALAB 250Xi system equipped with a monochromated Al K $\alpha$  source at 1486.6 eV. The XPS measurement area was  $\sim 500 \times 500 \mu\text{m}^2$ . During the measurement, a flood gun was operated for charge compensation. Additionally, an Ar<sup>+</sup> ion beam was used for depth profiling, operated at 3 kV, with 180 s etch time per etch level, and  $2.5 \times 2.5 \text{ mm}^2$  etch area. The data analysis was performed with CasaXPS, and the data were charge-corrected to the adventitious C 1s peak at 284.8 eV.

### Device design, Finite element modeling (FEM)

Each device is patterned into a TiN/ $\gamma$ -Al<sub>2</sub>O<sub>3</sub>/TiN PPC, shunted by an inductor made from the bottom TiN layer, forming a quasi-lumped-element resonator. From prior measurements of the oxide thickness, capacitor and inductor dimensions are carefully designed and simulated with Ansys HFSS to obtain resonance frequencies in the appropriate measurement range (4 – 8 GHz). Following the procedure described in McRae *et al.*<sup>44</sup>, we perform simulations to determine the shunting capacitance  $C_L$  and inductance  $L$  arising from the shunting inductor. The PPC area is then selected to achieve a capacitance  $C_C$  and resulting angular frequency  $\omega = 1/\sqrt{L(C_C + C_L)}$ . To directly measure the dielectric loss coming from the  $\gamma$ -Al<sub>2</sub>O<sub>3</sub> layer, we minimize the shunting capacitance such that the electric participation ratio in the capacitor,  $C_C/(C_C + C_L)$ , is over 0.99 in all devices. Assuming the inductor effective TLS loss tangent  $F_L \tan \delta_L$  is upper-bounded by  $10^{-4}$ , we estimate a systematic error in the extracted  $\gamma$ -Al<sub>2</sub>O<sub>3</sub> loss of under 2% from misattributing shunting capacitance loss to  $\gamma$ -Al<sub>2</sub>O<sub>3</sub>. This bound is motivated by the measured average TLS loss tangent of  $(5.8 \pm 0.4) \times 10^{-6}$  for CPW resonators patterned on the same chip as the aforementioned LEPPC devices (Fig. S5).

### Lumped-element resonator with parallel-plate capacitor (LEPPC) and air bridge fabrication

The LEPPC and air bridge fabrication procedure involves four rounds of photolithography using the optical mask shown in Fig. S3. For each round, the sample is spun coated with positive-tone photoresist (MICROPOSIT™ S1800™ series) and patterned by exposing with the Heidelberg  $\mu$ PG 501 maskless aligner and developing in AZ917 MIF. TiN layers are dry etched with fluorine chemistry using a SAMCO 10NR reactive ion etcher (RIE), while the  $\gamma$ -Al<sub>2</sub>O<sub>3</sub> layer is physically removed using an Ar<sup>+</sup> ion mill in the Plassys BESTEK MEB550SL4-UHV double-angle electron-beam evaporator, which is also used to deposit Al for the air bridges. Photoresists are stripped using N-methyl-2-pyrrolidone (NMP) at 70°C followed by rinses in acetone, isopropyl alcohol, and deionized water. Lastly, the samples are diced with Advanced Dicing Technologies 7122 wafer dicer and packaged using the Questar Q7800 automatic wedge bonder equipped with Al wire. Detailed device fabrication procedure can be found in the Supplementary Information.

### Dilution refrigerator (DR) measurement

Devices were measured in a cryogen-free dilution refrigerator with a base temperature of approximately 10 mK. Samples were mounted in gold-plated copper enclosures, wire-bonded, and

thermally anchored to the mixing chamber plate. The input microwave line included multiple stages of cryogenic attenuation and low-pass filtering to suppress thermal radiation and spurious high-frequency noise. The output line incorporated cryogenic isolators and a low-noise high-electron-mobility transistor amplifier at the 4 K stage, followed by additional amplification at room temperature. Scattering parameters were acquired using a vector network analyzer. This configuration enables quantitative measurements of SC resonators in the 4 – 8 GHz range down to excitation powers corresponding to sub-single-photon intracavity occupation. More details on the wiring configuration are given in Vallières *et al.*<sup>77</sup>

For each device, the complex resonator response was recorded as a function of input power at a fixed temperature. Individual resonance traces were analyzed using the diameter correction method, which accounts for systematic effects such as impedance mismatches, cable delays, and asymmetries in the microwave environment<sup>78, 79</sup>. This analysis yields the resonance frequency, internal quality factor  $Q_i$ , coupling quality factor  $Q_c$ , and an asymmetry parameter characterizing the impedance mismatch.

To quantify dielectric loss, the extracted internal quality factor was analyzed as a function of microwave drive power (Fig. S5) using a TLS loss model<sup>80</sup>. This approach separates the saturable TLS contribution from residual power-independent losses, providing an effective TLS loss tangent for each resonator. From the fitted TLS parameters, we place an upper bound on the intrinsic loss tangent of the  $\gamma$ -Al<sub>2</sub>O<sub>3</sub> dielectric.

### **Scanning electron microscopy (SEM)**

Top-down (0°) and tilted (45°) SEM imaging was performed at 3 kV using the Hitachi SU8700 UHR FEG-SEM. The images were collected using a combination of the in-chamber Everhart–Thornley detector collecting secondary electrons and an in-column detector collecting backscattered electrons.

### **Superconducting transition temperature ( $T_c$ ) characterization**

Electrical transport measurements on the PLD TiN were performed using a Quantum Design Dynacool physical properties measurement system (PPMS) in a four-probe geometry. The sample was wire-bonded to the sample puck using a home-built In-Au wire bonder.

### **Data Availability**

The data supporting the findings of this study can be found in the manuscript and Supplementary Information.

## **Acknowledgements**

The authors thank G. dos Santos and R. dos Reis from Northwestern University (NU) for guidance on STEM characterization, D. B. Buchholz from NU for helping to design the PLD process, Y. Lu from Fermilab for assistance with LEPPC device design, and C. R. McRae from Nord Quantique for guidance and discussions on microwave data analysis. This work was primarily supported by the U.S. Department of Energy, Office of Science, National Quantum Information Science Research Centers, Superconducting Quantum Materials and Systems Center (SQMS), under Contract No. 89243024CSC000002. Fermilab is operated by Fermi Forward Discovery Group, LLC under Contract No. 89243024CSC000002 with the U.S. Department of Energy, Office of Science, Office of High Energy Physics. This work made use of the EPIC (RRID: SCR\_026361), Keck-II (RRID: SCR\_026360), and NUFAB (RRID: SCR\_017779) facilities of Northwestern University's NUANCE Center, which has received support from the IIN and Northwestern's MRSEC program (NSF DMR-2308691). Research reported in this publication was supported in part by instrumentation provided by the Office of The Director, National Institutes of Health of the National Institutes of Health under Award Number S10OD026871. The content is solely the responsibility of the authors and does not necessarily represent the official views of the National Institutes of Health. This work made use of the NU XRD Facility (RRID: SCR\_017866) and the Pulsed Laser Deposition Facility (RRID: SCR\_017889), supported by the MRSEC program (NSF-DMR-2308691) and SHyNE (NSF ECCS-2025633). This work made use of the MLTOF Facility which has received support from the MRSEC Program (NSF DMR-2308691), the Center for Hierarchical Materials Design, and Northwestern University. This work made use of the Pritzker Nanofabrication Facility, part of the Pritzker School of Molecular Engineering at the University of Chicago, which receives support from SHyNE (NSF ECCS-2025633), a node of the NSF National Nanotechnology Coordinated Infrastructure (RRID: SCR\_022955).

## **References**

1. A. Shnirman, G. Schön and Z. Hermon, *Physical Review Letters* **79** (12), 2371-2374 (1997).
2. V. Bouchiat, D. Vion, P. Joyez, D. Esteve and M. H. Devoret, *Physica Scripta* **1998** (T76), 165 (1998).
3. Y. Nakamura, Y. A. Pashkin and J. S. Tsai, *Nature* **398** (6730), 786-788 (1999).
4. J. Koch, T. M. Yu, J. M. Gambetta, A. A. Houck, D. I. Schuster, J. Majer, A. Blais, M. H. Devoret, S. M. Girvin and R. J. Schoelkopf, *Physical Review A* **76** (4), 042319 (2007).
5. J. Lisenfeld, G. J. Grabovskij, C. Müller, J. H. Cole, G. Weiss and A. V. Ustinov, *Nature Communications* **6** (1), 6182 (2015).
6. C. Müller, J. H. Cole and J. Lisenfeld, *Reports on Progress in Physics* **82** (12), 124501 (2019).
7. J. M. Martinis, K. B. Cooper, R. McDermott, M. Steffen, M. Ansmann, K. D. Osborn, K. Cicak, S. Oh, D. P. Pappas, R. W. Simmonds and C. C. Yu, *Physical Review Letters* **95** (21), 210503 (2005).
8. J. Lisenfeld, A. Bilmes, S. Matityahu, S. Zanker, M. Marthaler, M. Schechter, G. Schon, A. Shnirman, G. Weiss and A. V. Ustinov, *Scientific Reports* **6**, 23786 (2016).
9. J. J. Burnett, A. Bengtsson, M. Scigliuzzo, D. Niepce, M. Kudra, P. Delsing and J. Bylander, *npj Quantum Information* **5** (1), 54 (2019).
10. L. Zeng, D. T. Tran, C. W. Tai, G. Svensson and E. Olsson, *Scientific Reports* **6**, 29679 (2016).
11. W. D. Oliver and P. B. Welander, *MRS Bulletin* **38** (10), 816-825 (2013).
12. A. P. McFadden, A. Goswami, M. Seas, C. R. H. McRae, R. Zhao, D. P. Pappas and C. J. Palmstrøm, *Journal of Applied Physics* **128** (11), 115301 (2020).
13. C. R. H. McRae, A. McFadden, R. Zhao, H. Wang, J. L. Long, T. Zhao, S. Park, M. Bal, C. J. Palmstrøm and D. P. Pappas, *Journal of Applied Physics* **129** (2), 025109 (2021).
14. Y. Nakamura, H. Terai, K. Inomata, T. Yamamoto, W. Qiu and Z. Wang, *Applied Physics Letters* **99** (21), 212502 (2011).
15. D. Wang, Y. Wu, N. Pieczulewski, P. Garg, M. C. C. Pace, C. G. L. Böttcher, B. Mazumder, D. A. Muller and H. X. Tang, *Nature Materials* (2026).
16. K. Fricke, *Journal of Applied Physics* **70** (2), 914-918 (1991).
17. M.-A. Dubois and P. Mural, *Applied Physics Letters* **74** (20), 3032-3034 (1999).
18. C. Sundahl, J. Makita, P. B. Welander, Y.-F. Su, F. Kametani, L. Xie, H. Zhang, L. Li, A. Gurevich and C.-B. Eom, *Scientific Reports* **11** (1), 7770 (2021).
19. P. B. Welander, PhD Thesis, University of Illinois at Urbana-Champaign, 2007.

20. K. H. Cho, U. Patel, J. Podkaminer, Y. Gao, C. M. Folkman, C. W. Bark, S. Lee, Y. Zhang, X. Q. Pan, R. McDermott and C. B. Eom, *APL Materials* **1** (4), 042115 (2013).
21. M. P. Weides, J. S. Kline, M. R. Vissers, M. O. Sandberg, D. S. Wisbey, B. R. Johnson, T. A. Ohki and D. P. Pappas, *Applied Physics Letters* **99** (26), 262502 (2011).
22. J. S. Kline, M. R. Vissers, F. C. S. D. Silva, D. S. Wisbey, M. Weides, T. J. Weir, B. Turek, D. A. Braje, W. D. Oliver, Y. Shalibo, N. Katz, B. R. Johnson, T. A. Ohki and D. P. Pappas, *Superconductor Science and Technology* **25** (2), 025005 (2012).
23. J. K. Hulm and B. B. Goodman, *Physical Review* **106** (4), 659-671 (1957).
24. D. Jena, R. Page, J. Casamento, P. Dang, J. Singhal, Z. Zhang, J. Wright, G. Khalsa, Y. Cho and H. G. Xing, *Japanese Journal of Applied Physics* **58** (SC), SC0801 (2019).
25. P. Dang, G. Khalsa, C. S. Chang, D. S. Katzer, N. Nepal, B. P. Downey, V. D. Wheeler, A. Suslov, A. Xie, E. Beam, Y. Cao, C. Lee, D. A. Muller, H. G. Xing, D. J. Meyer and D. Jena, *Science Advances* **7** (8), eabf1388 (2021).
26. A. Ithepalli, A. R. Rajapurohita, A. Singh, R. Singh, J. Wright, F. Rana, V. Fatemi, H. G. Xing and D. Jena, *Applied Physics Letters* **126** (22), 222601 (2025).
27. J. Sarker, P. Garg, M. Zhu, C. M. Rouleau, J. Hwang, E. Osei-Agyemang and B. Mazumder, *ACS Applied Engineering Materials* **1** (12), 3227-3236 (2023).
28. M. R. Vissers, J. Gao, D. S. Wisbey, D. A. Hite, C. C. Tsuei, A. D. Corcoles, M. Steffen and D. P. Pappas, *Applied Physics Letters* **97** (23), 232509 (2010).
29. J. B. Chang, M. R. Vissers, A. D. Corcoles, M. Sandberg, J. Gao, D. W. Abraham, J. M. Chow, J. M. Gambetta, M. B. Rothwell, G. A. Keefe, M. Steffen and D. P. Pappas, *Applied Physics Letters* **103** (1), 012602 (2013).
30. A. Melville, G. Calusine, W. Woods, K. Serniak, E. Golden, B. M. Niedzielski, D. K. Kim, A. Sevi, J. L. Yoder, E. A. Dauler and W. D. Oliver, *Applied Physics Letters* **117** (12), 124004 (2020).
31. A. Torgovkin, A. Ruhtinas and I. J. Maasilta, *IEEE Transactions on Applied Superconductivity* **31** (5), 1-4 (2021).
32. R. Gao, W. Yu, H. Deng, H. S. Ku, Z. Li, M. Wang, X. Miao, Y. Lin and C. Deng, *Physical Review Materials* **6** (3), 036202 (2022).
33. H. Deng, Z. Song, R. Gao, T. Xia, F. Bao, X. Jiang, H. S. Ku, Z. Li, X. Ma, J. Qin, H. Sun, C. Tang, T. Wang, F. Wu, W. Yu, G. Zhang, X. Zhang, J. Zhou, X. Zhu, Y. Shi, H. H. Zhao and C. Deng, *Physical Review Applied* **19** (2), 024013 (2023).

34. M. Bal, A. A. Murthy, S. Zhu, F. Crisa, X. You, Z. Huang, T. Roy, J. Lee, D. M. P. v. Zanten, R. Pilipenko, I. Nekrashevich, D. Bafia, Y. Krasnikova, C. J. Kopas, E. O. Lachman, D. Miller, J. Y. Mutus, M. J. Reagor, H. Cansizoglu, J. Marshall, D. P. Pappas, K. Vu, K. Yadavalli, J.-S. Oh, L. Zhou, M. J. Kramer, F. Q. Lecocq, D. P. Goronzy, C. G. Torres-Castanedo, G. Pritchard, V. P. Dravid, J. M. Rondinelli, M. J. Bedzyk, M. C. Hersam, J. Zasadzinski, J. Koch, J. A. Sauls, A. Romanenko and A. Grassellino, *npj Quantum Information* **10** (43), 1-8 (2024).
35. M.-A. Nicolet, *Thin Solid Films* **52** (3), 415-443 (1978).
36. R. A. Araujo, X. Zhang and H. Wang, *Journal of Vacuum Science & Technology B: Microelectronics and Nanometer Structures Processing, Measurement, and Phenomena* **26** (6), 1871-1874 (2008).
37. M. Göppl, A. Fragner, M. Baur, R. Bianchetti, S. Filipp, J. M. Fink, P. J. Leek, G. Puebla, L. Steffen and A. Wallraff, *Journal of Applied Physics* **104** (11), 113904 (2008).
38. R. Zhao, S. Park, T. Zhao, M. Bal, C. R. H. McRae, J. Long and D. P. Pappas, *Physical Review Applied* **14** (6), 064006 (2020).
39. H. J. Mamin, E. Huang, S. Carnevale, C. T. Rettner, N. Arellano, M. H. Sherwood, C. Kurter, B. Trimm, M. Sandberg, R. M. Shelby, M. A. Mueed, B. A. Madon, A. Pushp, M. Steffen and D. Rugar, *Physical Review Applied* **16** (2), 024023 (2021).
40. A. Antony, M. V. Gustafsson, G. J. Ribeill, M. Ware, A. Rajendran, L. C. G. Govia, T. A. Ohki, T. Taniguchi, K. Watanabe, J. Hone and K. C. Fong, *Nano Letters* **21** (23), 10122-10126 (2021).
41. J. I. J. Wang, M. A. Yamoah, Q. Li, A. H. Karamlou, T. Dinh, B. Kannan, J. Braumüller, D. Kim, A. J. Melville, S. E. Muschinske, B. M. Niedzielski, K. Serniak, Y. Sung, R. Winik, J. L. Yoder, M. E. Schwartz, K. Watanabe, T. Taniguchi, T. P. Orlando, S. Gustavsson, P. Jarillo-Herrero and W. D. Oliver, *Nature Materials* **21** (4), 398-403 (2022).
42. A. Torgovkin, S. Chaudhuri, A. Ruhtinas, M. Lahtinen, T. Sajavaara and I. J. Maasilta, *Superconductor Science and Technology* **31** (5), 055017 (2018).
43. G. Balakrishnan, R. V. Babu, K. S. Shin and J. I. Song, *Optics & Laser Technology* **56**, 317-321 (2014).
44. C. R. H. McRae, R. E. Lake, J. L. Long, M. Bal, X. Wu, B. Jugdersuren, T. H. Metcalf, X. Liu and D. P. Pappas, *Applied Physics Letters* **116** (19), 194003 (2020).
45. P. B. Welander, V. Bolkhovsky, T. J. Weir, M. A. Gouker and W. D. Oliver, (arXiv, 2012).

46. E. Smrčok, V. Langer and J. Křest'an, *Acta Crystallographica Section C: Crystal Structure Communications* **62** (9), i83-i84 (2006).
47. C. Merckling, M. El-Kazzi, G. Saint-Girons, G. Hollinger, L. Largeau, G. Patriarche, V. Favre-Nicolin and O. Marty, *Journal of Applied Physics* **102** (2), 024101 (2007).
48. D. Jaeger and J. Patscheider, *Journal of Electron Spectroscopy and Related Phenomena* **185** (11), 523-534 (2012).
49. L. Porte, L. Roux and J. Hanus, *Physical Review B* **28** (6), 3214-3224 (1983).
50. E. O. Filatova, A. S. Konashuk, S. S. Sakhonenkov, A. A. Sokolov and V. V. Afanas'ev, *Scientific Reports* **7** (1), 4541 (2017).
51. I. Bertóti, M. Mohai, J. L. Sullivan and S. O. Saied, *Applied Surface Science* **84** (4), 357-371 (1995).
52. I. Abdallah, C. Dupressoire, L. Laffont, D. Monceau and A. V. Put, *Corrosion Science* **153**, 191-199 (2019).
53. S. Toyoda, T. Shinohara, H. Kumigashira, M. Oshima and Y. Kato, *Applied Physics Letters* **101** (23), 231607 (2012).
54. I. Manassidis and M. J. Gillan, *Journal of the American Ceramic Society* **77** (2), 335-338 (1994).
55. H. O. Ayoola, C. H. Li, S. D. House, C. S. Bonifacio, K. Kisslinger, J. Jinschek, W. A. Saidi and J. C. Yang, *Ultramicroscopy* **219**, 113127 (2020).
56. E. O. Filatova, A. S. Konashuk, F. Schaefer and V. V. Afanas'ev, *The Journal of Physical Chemistry C* **120** (16), 8979-8985 (2016).
57. Z. Chen, A. Megrant, J. Kelly, R. Barends, J. Bochmann, Y. Chen, B. Chiaro, A. Dunsworth, E. Jeffrey, J. Y. Mutus, P. J. J. O'Malley, C. Neill, P. Roushan, D. Sank, A. Vainsencher, J. Wenner, T. C. White, A. N. Cleland and J. M. Martinis, *Applied Physics Letters* **104** (5), 052602 (2014).
58. J. Zotova, R. Wang, A. Semenov, Y. Zhou, I. Khrapach, A. Tomonaga, O. Astafiev and J.-S. Tsai, *Physical Review Applied* **19** (4), 044067 (2023).
59. G. Hammer, S. Wuensch, K. Ilin and M. Siegel, *Journal of Physics: Conference Series* **97**, 012044 (2008).
60. S. Beldi, F. Boussaha, J. Hu, A. Monfardini, A. Traini, F. Levy-Bertrand, C. Chaumont, M. Gonzales, J. Firminy, F. Reix, M. Rosticher, S. Mignot, M. Piat and P. Bonifacio, *Optics Express* **27** (9), 13319 (2019).
61. C. Deng, M. Otto and A. Lupascu, *Applied Physics Letters* **104** (4), 043506 (2014).

62. J. D. Brehm, A. Bilmes, G. Weiss, A. V. Ustinov and J. Lisenfeld, *Applied Physics Letters* **111** (11), 112601 (2017).
63. C. Kaiser, S. T. Skacel, S. Wunsch, R. Dolata, B. Mackrodt, A. Zorin and M. Siegel, *Superconductor Science and Technology* **23** (7), 075008 (2010).
64. K. Cicak, D. Li, J. A. Strong, M. S. Allman, F. Altomare, A. J. Sirois, J. D. Whittaker, J. D. Teufel and R. W. Simmonds, *Applied Physics Letters* **96** (9), 093502 (2010).
65. F. Lecocq, L. Ranzani, G. A. Peterson, K. Cicak, R. W. Simmonds, J. D. Teufel and J. Aumentado, *Physical Review Applied* **7** (2), 024028 (2017).
66. J. Sun, S. Shu, Y. Chai, L. Zhu, L. Zhang, Y. Li, Z. Liu, Z. Li, W. Shi, Y. Xu, D. Yan, W. Guo, Y. Wang and C. Liu, *Journal of Low Temperature Physics* **217** (3-4), 464-471 (2024).
67. A. Goswami, A. P. McFadden, T. Zhao, H. Inbar, J. T. Dong, R. Zhao, C. R. H. McRae, R. W. Simmonds, C. J. Palmstrøm and D. P. Pappas, *Applied Physics Letters* **121** (6), 064001 (2022).
68. S. J. Weber, K. W. Murch, D. H. Slichter, R. Vijay and I. Siddiqi, *Applied Physics Letters* **98** (17), 172510 (2011).
69. A. D. O'Connell, M. Ansmann, R. C. Bialczak, M. Hofheinz, N. Katz, E. Lucero, C. McKenney, M. Neeley, H. Wang, E. M. Weig, A. N. Cleland and J. M. Martinis, *Applied Physics Letters* **92** (11), 112903 (2008).
70. K. Kouwenhoven, G. P. J. v. Doorn, B. T. Buijtenorp, S. A. H. d. Rooij, D. Lamers, D. J. Thoen, V. Murugesan, J. J. A. Baselmans and P. J. d. Visser, *Physical Review Applied* **21** (4), 044036 (2024).
71. J. C. Hood II, P. S. Barry, T. Cecil, C. L. Chang, J. Li, S. S. Meyer, Z. Pan, E. Shirokoff and A. Tang, *Journal of Low Temperature Physics* **209** (5-6), 1189-1195 (2022).
72. H. Paik and K. D. Osborn, *Applied Physics Letters* **96** (7), 072505 (2010).
73. B. Sarabi, A. N. Ramanayaka, A. L. Burin, F. C. Wellstood and K. D. Osborn, *Physical Review Letters* **116** (16), 167002 (2016).
74. Z. Pan, P. S. Barry, T. Cecil, C. Albert, A. N. Bender, C. L. Chang, R. Gualtieri, J. Hood, J. Li, J. Zhang, M. Lisovenko, V. Novosad, G. Wang and V. Yefremenko, *IEEE Transactions on Applied Superconductivity* **33** (5), 1101707 (2023).
75. S. T. Skacel, C. Kaiser, S. Wunsch, H. Rotzinger, A. Lukashenko, M. Jerger, G. Weiss, M. Siegel and A. V. Ustinov, *Applied Physics Letters* **106** (2), 022603 (2015).
76. A. R. J. Nelson and S. W. Prescott, *Journal of Applied Crystallography* **52** (1), 193-200 (2019).

77. A. Vallières, M. E. Russell, X. You, D. A. Garcia-Wetten, D. P. Goronzy, M. J. Walker, M. J. Bedzyk, M. C. Hersam, A. Romanenko, Y. Lu, A. Grassellino, J. Koch and C. R. H. McRae, *Applied Physics Letters* **126** (124001), 124001 (2025).
78. M. S. Khalil, M. J. A. Stoutimore, F. C. Wellstood and K. D. Osborn, *Journal of Applied Physics* **111** (5), 054510 (2012).
79. P. G. Baity, C. Maclean, V. Seferai, J. Bronstein, Y. Shu, T. Hemakumara and M. Weides, *Physical Review Research* **6** (1), 013329 (2024).
80. C. R. H. McRae, H. Wang, J. Gao, M. R. Vissers, T. Brecht, A. Dunsworth, D. P. Pappas and J. Mutus, *Review of Scientific Instruments* **91** (9), 091101 (2020).

## **Author Information**

These authors contributed equally: David A. Garcia-Wetten, Mitchell J. Walker, Peter G. Lim.

## **Contributions**

D.A.G.-W. and M.J.W. conceived the project with contributions from P.G.L. and A.V. D.A.G.-W., M.J.W. and P.G.L. designed the experiments for materials analysis. D.A.G.-W. deposited the materials stack using PLD with contributions from M.G.J.-G. D.A.G.-W. performed X-ray characterization. P.G.L. performed electron microscopy characterization with contributions from M.A.A. M.J.W. performed XPS, ToF-SIMS, and PPMS characterization with contributions from D.A.G.-W. and D.P.G. A.V. designed the devices and performed microwave measurements in the DR. M.J.W. fabricated the devices with contributions from D.A.G.-W. and P.G.L. D.A.G.-W., M.J.W. and P.G.L. wrote the manuscript with input from all other authors. D.P.G., A.G., J.K., V.P.D., M.C.H. and M.J.B. supervised the project.

## **Corresponding authors**

Correspondence to Vinayak P. Dravid, Mark C. Hersam, or Michael J. Bedzyk.

## **Ethics Declaration**

### **Competing interests**

The authors declare no competing interests.

Supplementary Information for:

**Oxide-nitride heteroepitaxy for low-loss dielectrics in superconducting quantum circuits**

David A. Garcia-Wetten<sup>1,\*</sup>, Mitchell J. Walker<sup>1,\*</sup>, Peter G. Lim<sup>2,\*</sup>, André Vallières<sup>2,3</sup>, Maria G. Jimenez-Guillermo<sup>1,4</sup>, Miguel A. Alvarado<sup>5</sup>, Dominic P. Goronzy<sup>1</sup>, Anna Grassellino<sup>3</sup>, Jens Koch<sup>6,7</sup>, Vinayak P. Dravid<sup>1,8,9,†</sup>, Mark C. Hersam<sup>1,10,11,†</sup>, Michael J. Bedzyk<sup>1,6,†</sup>

<sup>1</sup>Department of Materials Science and Engineering, Northwestern University, Evanston, IL 60208, USA

<sup>2</sup>Graduate Program in Applied Physics, Northwestern University, Evanston, IL 60208, USA

<sup>3</sup>Superconducting Quantum Materials and Systems (SQMS) Division, Fermi National Accelerator Laboratory (FNAL), Batavia, IL 60510, USA

<sup>4</sup>Department of Physics, Elmhurst University, Elmhurst, IL 60126, USA

<sup>5</sup>Department of Chemistry, Northeastern Illinois University, Chicago, IL 60625, USA

<sup>6</sup>Department of Physics and Astronomy, Northwestern University, Evanston, IL 60208, USA

<sup>7</sup>Center for Applied Physics and Superconducting Technologies (CAPST), Northwestern University, Evanston, IL 60208, USA

<sup>8</sup>Northwestern University Atomic and Nanoscale Characterization Experimental (NUANCE) Center, Northwestern University, Evanston, IL 60208, USA

<sup>9</sup>International Institute of Nanotechnology (IIN), Northwestern University, Evanston, IL 60208, USA

<sup>10</sup>Department of Chemistry, Northwestern University, Evanston, IL 60208, USA

<sup>11</sup>Department of Electrical and Computer Engineering, Northwestern University, Evanston, IL 60208, USA

\*These authors contributed equally to this work.

†Corresponding authors: v-dravid@northwestern.edu, m-hersam@northwestern.edu, bedzyk@northwestern.edu

## I. Additional characterization of trilayer crystal structure with 4D-STEM

4D-STEM measurements are employed to characterize the structure of each layer in the trilayer stack and its interfaces precisely. Fig. S1a is a virtual bright-field image of the thin  $\gamma$ - $\text{Al}_2\text{O}_3$  sample, where the colored rectangles correspond to nanobeam electron diffraction (NBED) patterns collected at those regions, alongside simulated diffraction patterns (Figs. S1b-e). These diffraction patterns serve as additional confirmation that there is TiN (111) epitaxial growth on sapphire (001) (Fig. S1b); that the majority of the TiN layers are oriented in the (111) specular orientation (Fig. S1c); and that the crystal structure of the dielectric  $\text{Al}_2\text{O}_3$  is the cubic  $\gamma$ -phase (Fig. S1e). However, in some regions of the top TiN (Fig. S1d), the diffraction patterns show reflections from a TiN  $180^\circ$  twin domain in the (002) specular orientation. Virtual dark-field images obtained from the  $\{111\}$  (Fig. S1f) and  $\{002\}$  family of reflections (Fig. S1g) confirm the presence of two distinct domains corresponding to these diffraction spots.

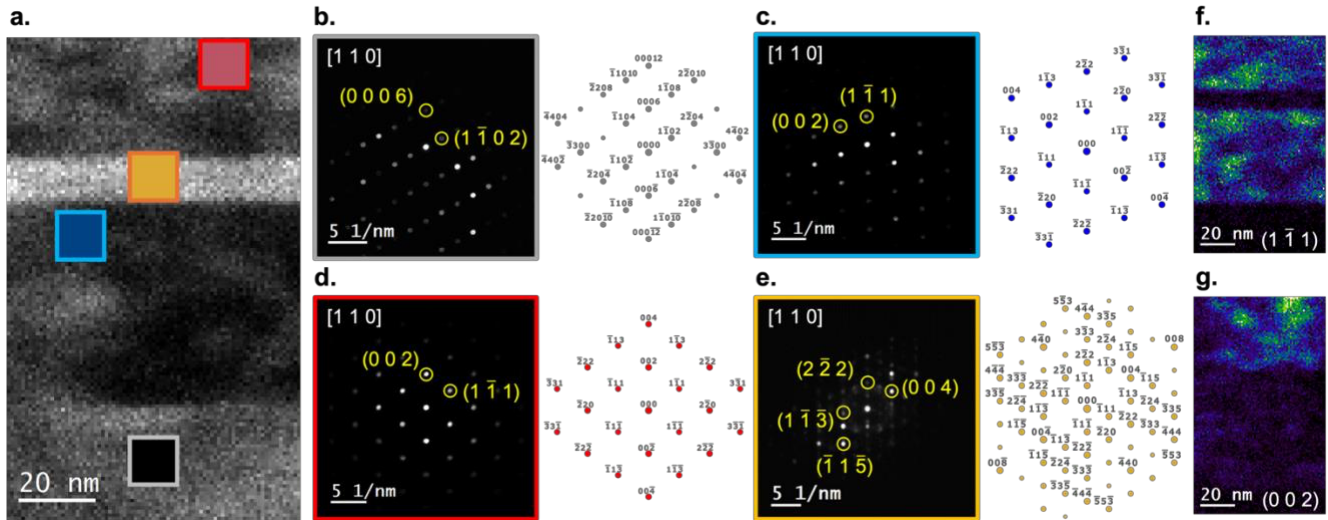


**Fig. S1: 4D-STEM characterization of the epitaxial trilayer.**

**a**, Diffraction spectrum image of the thin trilayer sample. The colored boxes indicate the regions in which **b-e**, NBED patterns of the various layers were collected, confirming the crystal structure and orientation of the TiN layers and the  $\gamma$ -phase  $\text{Al}_2\text{O}_3$  as previously shown in Fig. 2. **f-g**, Virtual dark-field images of the  $(1\bar{1}1)$  and the  $(002)$  out-of-plane orientations of TiN, indicating the spatial distribution of the  $180^\circ$  twin domains.

**II. Superconducting properties of PLD-grown TiN**

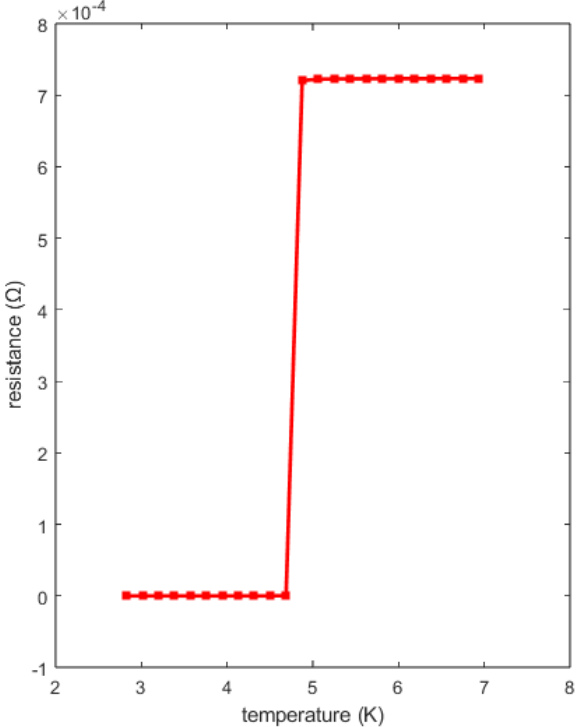


**Fig. S2: Superconducting transition temperature of TiN.**

Plot of resistance vs. temperature of PLD-deposited TiN as measured using the Quantum Design PPMS. The superconducting transition temperature is extracted to be 4.8 K, as expected.

### III. Detailed device fabrication procedure

The LEPPC and air bridge fabrication procedure involves four rounds of photolithography using the optical mask shown in Fig. S3. Starting with a blanket film of epitaxial TiN/ $\gamma$ -Al<sub>2</sub>O<sub>3</sub>/TiN/ $\alpha$ -Al<sub>2</sub>O<sub>3</sub>, S1813 photoresist was spun onto the sample at 5000 rpm and then baked at 110°C for 60 s. The photoresist was then patterned into circles to define the shape of the circular capacitor pads, by exposing it with a Heidelberg  $\mu$ PG 501 maskless aligner and developing in AZ917 MIF developer for 40 s, with no agitation.

The top TiN layer was then etched using a SAMCO 10NR reactive ion etcher (RIE). The RIE process consisted of a 10 s descum step with 20 sccm of O<sub>2</sub>, at 10 Pa and 60 W RF power, followed by 8 min of etching in SF<sub>6</sub> at 30 sccm, 2 Pa, and 40 W RF power.

The samples were then loaded into a Plassys BESTEK MEB550SL4-UHV double-angle electron-beam evaporator with an *in situ* ion mill. Using the same photoresist patterned into circular capacitor pads, the Al<sub>2</sub>O<sub>3</sub> layer of the trilayer was etched away with Ar<sup>+</sup> ion milling at 6 sccm gas flow, 400 V anode voltage, and 24 mA emitter current. The thick Al<sub>2</sub>O<sub>3</sub> layer required 70.3 min of milling to etch through, and the thin Al<sub>2</sub>O<sub>3</sub> layer required 18 min.

The samples were then loaded into the previously described Thermo Scientific ESCALAB 250Xi. XPS data in the region of Al 2p were collected to verify the absence of any Al remaining on the surface. The photoresist patterned into the shape of circular capacitor pads was then removed by dissolving it in N-methyl-2-pyrrolidone (NMP) at 70°C.

To define the lumped-element resonators, S1805 photoresist was spun onto the samples at 5000 rpm, and subsequently baked at 110°C for 60 s. The photoresist was then patterned into the shape of lumped-element resonators by aligning and exposing it with a Heidelberg  $\mu$ PG 501 maskless aligner and developing in AZ917 MIF developer for 40 s, with no agitation. In addition to the lumped-element resonators, this photomask also contains two CPW resonators coupled to the feedline.

The bottom TiN layer was then etched using a SAMCO 10NR RIE. The RIE recipe consisted of a 10 s descum step with 20 sccm of O<sub>2</sub>, a pressure of 10 Pa, and a RF power of 60 W, followed by 8 min of etching in SF<sub>6</sub> at 30 sccm, 2 Pa, and 40 W. The photoresist patterned into the shape of lumped-element resonators was then removed by dissolving it in NMP at 70°C.

Next, air bridges were fabricated on the LEPPC devices according to a technique inspired by Chen *et al.*<sup>57</sup> S1813 photoresist was spun onto the piece at 5000 rpm and then baked at 110°C for 60 s. The photoresist was then patterned into the shape of air-bridge base regions by aligning and exposing it with

a Heidelberg  $\mu$ PG 501 maskless aligner and developing in AZ917 MIF developer for 40 s, with no agitation. The photoresist was then reflowed by baking at 150°C for 60 s.

The samples were then transferred to the Plassys BESTEK MEB550SL4-UHV double-angle electron-beam evaporator with an *in situ* ion mill. The samples were exposed to the Ar<sup>+</sup> ion gun for 30 s at 6 sccm, 400 V anode voltage, and 24 mA emitter current to remove any adventitious contaminants and Ti<sub>x</sub>O<sub>y</sub>N<sub>z</sub> on the surface, thereby achieving good contact between the air-bridge Al and the TiN layers (Fig. S4). Then, without breaking vacuum, 300 nm of Al was deposited onto the samples at 0.4 nm/s.

The samples were then removed from the vacuum, and S1805 photoresist was spun onto them at 5000 rpm, followed by a 60 s bake at 110 °C. The photoresist was then patterned into the shape of air bridges by aligning and exposing it with a Heidelberg  $\mu$ PG 501 maskless aligner and developing in AZ917 MIF developer for 40 s, with no agitation.

The exposed Al was then etched away by dipping the samples into Transene Al etchant type A at 50°C until a color change associated with the disappearance of the Al was observed. The samples were then rinsed with deionized water and dipped in NMP at 70°C to remove the remaining photoresist. The samples were then transferred to a SAMCO PC-300 plasma cleaner and exposed to oxygen plasma for 3 min to remove any remaining photoresist residue after the NMP treatment.

Next, the devices were coated with S1805 photoresist spun at 5000 rpm to protect them during dicing. The samples were diced with the Advanced Dicing Technologies 7122 wafer dicer. The protective photoresist was then removed by dissolving in NMP at 70°C.

The devices were wire-bonded to microwave packages made of gold-plated high-purity copper using a Questar Q7800 automatic wedge bonder equipped with Al wire. The devices were then loaded into an Oxford Instruments ProteoxMX dilution refrigerator for cryogenic measurement, the results of which are shown in Fig. S5.

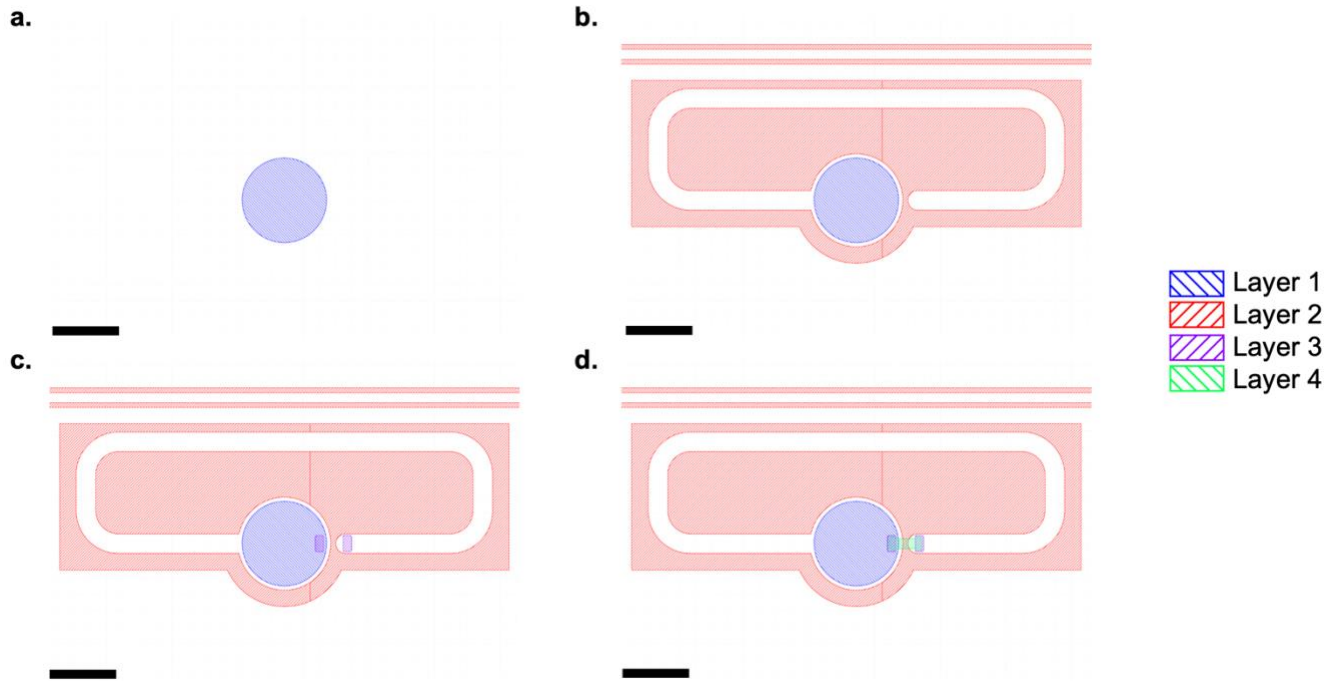


**Fig. S3: Photomask patterns for LEPPC lithography.**

Photomask patterns for each of the four photolithography steps involved in the fabrication of **a**, the PPC, **b**, the LE resonator and feedline, **c**, base layers for the airbridge, and **d**, protective layers for the airbridge. The scale bars are all 40  $\mu\text{m}$ , and the legend applies to all panels of the figure. The polarity of layers 1 and 4 have been inverted for clarity.

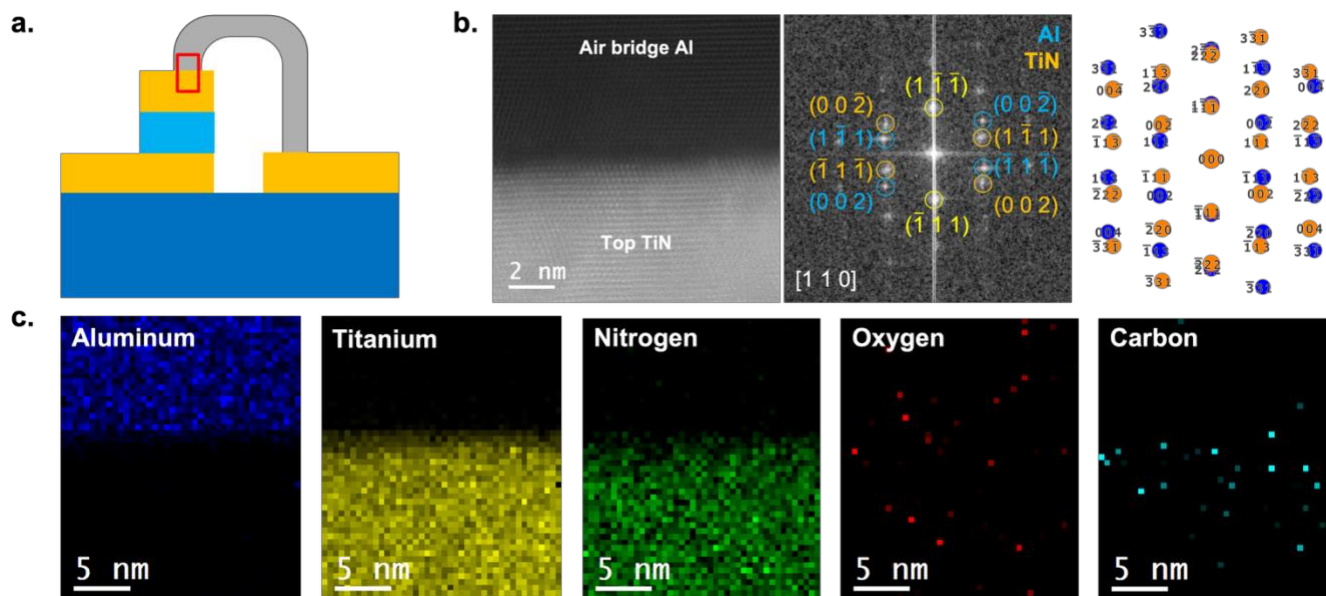


**Fig. S4: Characterization of the Al airbridge-TiN PPC interface.**

**a,** Schematic of the full LEPPC device. The red box indicates the airbridge-PPC interface region analyzed using STEM and EDS. **b,** HAADF-STEM image, FFT pattern, and simulated diffraction patterns of Al (blue) and TiN (orange) at the airbridge-PPC interface. The interface is generally flat, and the indexed FFT peaks demonstrate lattice matching between the two layers. **c,** EDS maps of relevant elements, showing minimal oxygen and carbon contamination along the interface.

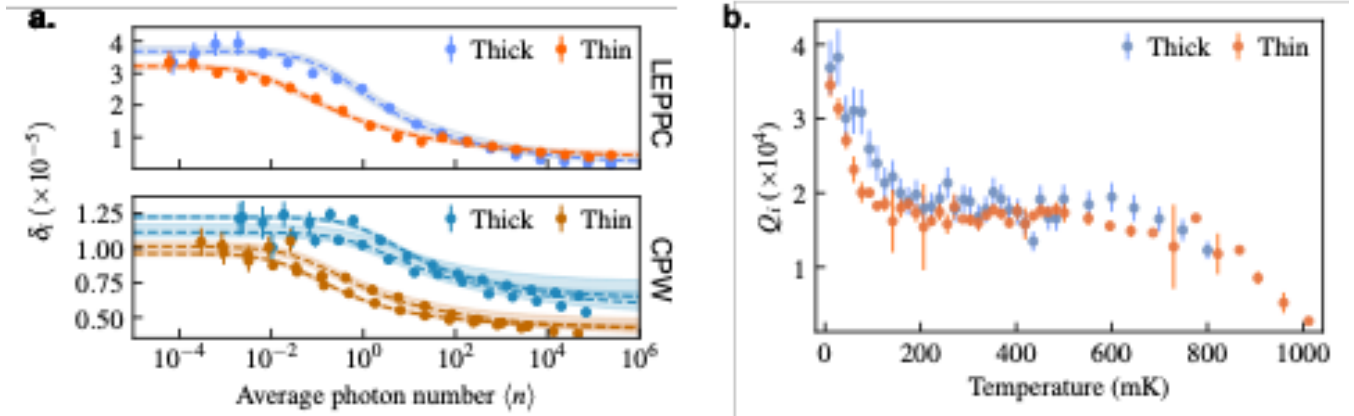


**Fig. S5: Cryogenic microwave measurement results of the resonators.**

**a**, Power-dependent intrinsic loss  $\delta_i = 1/Q_i$  for LEPPC (top) and CPW (bottom) resonators patterned on the bottom TiN layer of the thick (blue) and thin (orange) dielectric devices. Shaded bands represent uncertainty derived from the covariance matrix of each fit. **b**, Temperature-dependent intrinsic quality factor  $Q_i$  at low power for the LEPPC devices. Interesting features that warrant future investigations include the absence of any increase of  $Q_i$  from two-level systems saturation at increasing temperature, the plateau at around 200 mK - 600 mK, and differences between the thick (blue) and thin (orange) dielectric devices.

#### IV. Extended discussion on Table I

Table I of the main text serves as a comparison of microwave loss properties of  $\gamma$ -Al<sub>2</sub>O<sub>3</sub> to other notable dielectrics reported in the literature. Comparisons are limited to dielectrics measured in an integrated PPC-type geometry; nevertheless, a wide variety of dielectrics are included in terms of material, deposition technique, and crystallinity for completeness. Since researchers inevitably report different metrics based on their studies' contexts and applications, there are nuances that need to be considered for meaningful and accurate comparisons. We discuss some of those fine distinctions here.

As shown in Fig. S5, the low-power regime of this work corresponds to sub-single-photon intracavity occupations relevant for qubit applications, while the high-power regime reaches the  $\langle n \rangle \sim 10^5 - 10^6$  range, before the resonator response becomes nonlinear. However, how other researchers define “low-” and “high-power” can vary significantly, making blind comparisons of reported performance meaningless. For example, Beldi *et al.*<sup>1</sup> report an exceptionally low “low-power” loss tangent of  $\tan \delta_i \sim 6.6 \times 10^{-6}$  for their atomic layer deposited Al<sub>2</sub>O<sub>3</sub>; however, these measurements are not analogous to those of this work, for at least two reasons. First, their measurements were collected at  $T \sim 72$  mK, so it is plausible that many of the TLSs were saturated by the thermal energy. Second, and perhaps more importantly, their “low-power” is measured at a feedline power  $P \sim -100$  dBm with a resonance  $f \sim 1$  GHz, which translates to  $\langle n \rangle \sim 10^6$ . While this is the regime relevant for KID applications, this would mean their low-power measurements are more comparable to our high-power measurements, where TLSs are mostly saturated. This is why their results are presented in the  $Q_{max}$  column. Another omission from Table I are low-power measurements from Kaiser *et al.*<sup>2</sup>, who report “low-power” data measured at a generator power  $P \sim -27$  dBm, which more closely resembles high-power measurements in our work. However, we also note that since they measure at  $T \sim 4.2$  K, power is unlikely to be a factor here, as TLSs are likely saturated at this temperature regardless of power. Hence, what they measure is likely classical dielectric loss. For these reasons, data reported by all references are organized such that low-power  $\delta_{LP}$  measurements correspond to the single- or sub-single-photon regime on the order of  $\langle n \rangle \leq 10^0$ , while high-power  $Q_{max}$  data are those measured beyond the single-photon regime on the order of  $\langle n \rangle \geq 10^1$ , but mostly on the order of  $10^5 - 10^6$ .

The result presented in this work is an accurate estimate of the intrinsic material loss of  $\gamma$ -Al<sub>2</sub>O<sub>3</sub>. This is because the LEPPC devices have been carefully designed and simulated (Fig. 4d) so that the filling factor approaches 1 (for additional details, the readers are directed to the Methods section). Moreover, the

volume of the dielectric layer in these devices is large enough that the number of TLSs present will be similar to the theoretical TLS density for bulk  $\gamma$ -Al<sub>2</sub>O<sub>3</sub>.

However, for many of the references in Table I, devices serve a range of applications, so the geometries, filling factors, and/or TLS densities will also vary greatly. For example, Beldi *et al.*<sup>1</sup> perform their measurements on LEKID devices, for which not all of the electric field is in the capacitor, so their measurements may not be an accurate representation of the dielectric loss tangent. Mamin *et al.*<sup>3</sup> determined an even smaller loss tangent of  $\delta_i \lesssim 5 \times 10^{-7}$  for their electron-beam deposited AlO<sub>x</sub> in Al-AlO<sub>x</sub>-Al mergemons. However, a key reason for why their loss value was so low was the exceptionally small volume (dielectric thickness of 2 nm with an area of 1.4  $\mu\text{m}^2$ ) of their tunnel barrier, such that they could minimize the number of TLSs in the junction. As for Brehm *et al.*<sup>4</sup>, who report a  $F\delta_{\text{TLS}}^0$  as low as  $4 \times 10^{-5}$  for amorphous AlO<sub>x</sub>, their study is mainly focused on using applied mechanical strain to tune TLSs and thereby to study TLS ensemble effects; as a result, their measurement is not a pure measurement of the dielectric's loss and is not directly comparable to this work's result. Moreover, their device is more similar to a standard distributed CPW resonator, and a large portion of the loss may come from base metal surface oxides and defects, beyond AlO<sub>x</sub>.

## **References**

1. S. Beldi, F. Boussaha, J. Hu, A. Monfardini, A. Traini, F. Levy-Bertrand, C. Chaumont, M. Gonzales, J. Firminy, F. Reix, M. Rosticher, S. Mignot, M. Piat and P. Bonifacio, *Optics Express* **27** (9), 13319 (2019).
2. C. Kaiser, S. T. Skacel, S. Wünsch, R. Dolata, B. Mackrodt, A. Zorin and M. Siegel, *Superconductor Science and Technology* **23** (7), 075008 (2010).
3. H. J. Mamin, E. Huang, S. Carnevale, C. T. Rettner, N. Arellano, M. H. Sherwood, C. Kurter, B. Trimm, M. Sandberg, R. M. Shelby, M. A. Mueed, B. A. Madon, A. Pushp, M. Steffen and D. Rugar, *Physical Review Applied* **16** (2), 024023 (2021).
4. J. D. Brehm, A. Bilmes, G. Weiss, A. V. Ustinov and J. Lisenfeld, *Applied Physics Letters* **111** (11), 112601 (2017).